The Astrophysical Journal, 962:60 (18pp), 2024 February 10 https://doi.org/10.3847/1538-4357/ad17bc

Cosmological Distance Measurement of Twelve Nearby Supernovae IIP with ROTSE-IIIb

G. Dhungana[1], R. Kehoe[1], R. Staten[1], J. Vinko[2,3,4,5], J. C. Wheeler[2], C. Akerlof[6], D. Doss[7], F. V. Ferrante[1], C. A. Gibson[7], J. Lasker[1], G. H. Marion[2], S. B. Pandey[8], R. M. Quimby[9,10], E. Rykoff[11], D. Smith[12], F. Yuan[6], and W. Zheng[6,11]

[1] Department of Physics, Southern Methodist University, Dallas, TX, USA; gdhungana@smu.edu
[2] Department of Astronomy, University of Texas at Austin, 2515 Speedway, Stop C1400, Austin, Texas 78712-1205, USA
[3] CSFK Konkoly Observatory, Budapest, Konkoly-Thege M. ut 15-17, 1121, Hungary
[4] Department of Optics and Quantum Electronics, University of Szeged, Dom ter 9, Szeged, 6720 Hungary
[5] ELTE Eötvös Loránd University, Institute of Physics, Pázmány Péter sétány 1/A, Budapest, 1117 Hungary
[6] Department of Physics, University of Michigan, Ann Arbor, MI, USA
[7] McDonald Observatory, University of Texas at Austin, TX, USA
[8] Aryabhatta Research Institute of Observational Sciences (ARIES), Manora Peak, Nainital, Uttarakhand, 263001, India
[9] Department of Astronomy/Mount Laguna Observatory, San Diego State University, 5500 Campanile Drive, San Diego, CA, USA
[10] Kavli Institute for the Physics and Mathematics of the Universe (WPI), The University of Tokyo Institutes for Advanced Study, The University of Tokyo, Kashiwa, Chiba 277-8583, Japan
[11] Department of Astronomy, University of California, Berkeley, California, USA
[12] Guilford College, USA

Received 2023 July 31; revised 2023 December 15; accepted 2023 December 19; published 2024 February 7

Abstract

We present cosmological analysis of 12 nearby ($z < 0.06$) Type IIP supernovae (SNe IIP) observed with the ROTSE-IIIb telescope. To achieve precise photometry, we present a new image-differencing technique that is implemented for the first time on the ROTSE SN photometry pipeline. With this method, we find up to a 20% increase in the detection efficiency and significant reduction in residual rms scatter of the SN lightcurves when compared to the previous pipeline performance. We use the published optical spectra and broadband photometry of well-studied SNe IIP to establish temporal models for ejecta velocity and photospheric temperature evolution for our SNe IIP population. This study yields measurements that are competitive with other methods even when the data are limited to a single epoch during the photospheric phase of SNe IIP. Using the fully reduced ROTSE photometry and optical spectra, we apply these models to the respective photometric epochs for each SN in the ROTSE IIP sample. This facilitates the use of the Expanding Photosphere Method (EPM) to obtain distance estimates to their respective host galaxies. We then perform cosmological parameter fitting using these EPM distances, from which we measure the Hubble constant to be $72.9^{+5.7}_{-4.3}$ km s^{-1} Mpc^{-1}, which is consistent with the standard ΛCDM model values derived using other independent techniques.

Unified Astronomy Thesaurus concepts: Galaxies (573); Supernovae (1668); Distance measure (395); CCD photometry (208); Spectroscopy (1558); Type II supernovae (1731); Astronomy image processing (2306)

1. Introduction

Supernova (SN) cosmology has matured over the past few decades. Supernovae (SNe) have proven to be excellent distance indicators for astronomy and cosmology, due to their enormous and standardizable intrinsic brightness. Specifically, the improvements in the methods to precisely calibrate distances using the luminosities of SNe Ia remain in the forefront of SN cosmology. With the arrival of deeper surveys, these methods are being tested at even higher redshifts, and will prove complementary to other high-redshift cosmological probes such as baryon acoustic oscillations (BAO), cosmic microwave background (CMB), and weak lensing (see Weinberg et al. 2013; Nicola et al. 2017 for a review). While SNe Ia yield remarkable precision for the distance calibration based on their peak luminosity and lightcurve width relation (e.g., Phillips 1993; Riess et al. 1998; Tripp 1998; Perlmutter et al. 1999; DES Collaboration et al. 2018; Brout et al. 2022), there remain questions about the potential impact of discrepancies between the SN Ia models and the actual physical processes occuring (Benetti et al. 2005; Howell 2011; Marion et al. 2016; Blondin et al. 2017).

SNe IIP are continuously gaining interest as a standardizable candle population that provides a potent alternative class of distance indicators. The SNe IIP are believed to arise from the catastrophic gravitational collapse of the iron core of massive stars that have retained a substantial hydrogen envelope even at the time of collapse (e.g., Branch & Wheeler 2017, Ch. 12; Dhungana 2018). Because the explosion mechanism as well as the radiative transfer in SNe IIP are believed to be better understood than SNe Ia, the distance estimation is expected to be less affected by the systematic uncertainties due to explosion physics (e.g., Eastman et al. 1996). While SNe Ia may exhibit higher absolute luminosity, SNe IIP explosions also offer tremendous luminosity and occur more frequently than SNe Ia (e.g., (Graur et al. 2015)), presenting themselves as competitive distance indicators over an extensive redshift baseline. While these SNe show substantial diversity in their photometric and spectroscopic properties (Filippenko 1997; Hatano et al. 1999; Faran et al. 2014; Dhungana et al. 2016; Valenti et al. 2016;

Branch & Wheeler 2017), strong correlations in photometric and spectroscopic observables during the recombination phase can be exploited to provide a distance calibration. Several methods have been proposed over the last few decades to make the SNe IIP distance measurements calibratable. These methods are generally driven by the correlations of the luminosity with the expansion velocities. The pioneering work of Kirshner & Kwan (1974) using the Expanding Photosphere Method (EPM) treated SN IIP as a homologously expanding photosphere that emits light as a blackbody diluted from atmospheric scattering. This method relies on both the photometry and spectroscopy, where the observed flux is compared to the effective blackbody flux in the SN rest frame during the photospheric expansion phase of the SNe IIP. Using the models for the dilution correction factor (e.g., Eastman et al. 1996; Dessart & Hillier 2005), the EPM technique has been applied to numerous SNe IIP from independent samples (e.g., Schmidt et al. 1994; Hamuy et al. 2001; Jones et al. 2009; Vinkó et al. 2012; Bose & Kumar 2014; Dhungana et al. 2016; Gall et al. 2016). A close variant based on the correlations of luminosity with the expansion velocity at 50d after explosion was suggested and used as the Standardized Candle Method (SCM; e.g., Hamuy & Pinto 2002; Nugent et al. 2006; D'Andrea et al. 2010; Poznanski et al. 2010; de Jaeger et al. 2017; Gall et al. 2018; Szalai et al. 2019; Van Dyk et al. 2019; Vogl et al. 2019; Dong et al. 2021). The method has been further generalized (e.g, Kasen & Woosley 2009) to all epochs in the photospheric phase of the events. A newer technique called the Photospheric Magnitude Method (PMM; e.g., Rodríguez et al. 2014) is based on empirical color-based calibrations for the distance. Rodríguez et al. (2019) used the PMM technique in the near-IR bands where the effects from the dust and line contamination are much smaller compared to the optical wavelengths. de Jaeger et al. (2015) suggested a purely photometric technique called the Photometric Color Method (PCM) that requires no spectroscopy, unlike previous techniques.

It is important to test and improve these methods as we discover more SNe IIP at higher redshifts. These studies involving limited samples of SNe IIP at lower redshifts show promising signs of them providing independent and competitive distance estimates.

We present a cosmological analysis using distances of 12 SNe IIP that were observed by the ROTSE-III telescopes during the 2004–2013 survey period. Distances are derived using the EPM technique and primarily based only on ROTSE photometry and coordinated optical spectroscopy. This paper is organized as follows. In Section 2, we describe the photometric and spectroscopic data obtained for our SNe IIP sample. Section 3 describes the data reduction based on a new, improved image-differencing technique, along with photometric calibrations, spectroscopy, and *k*-corrections. In Section 4, we summarize the mathematical framework for the EPM. Section 5 discusses the photometric and spectroscopic parameters for the EPM and establishes their time-evolution models. The EPM distance measurements are discussed in Section 6. Section 7 presents the cosmological analysis and the Hubble diagram for our SNe IIP sample. We present the results and discussion in Section 8 and finally our conclusions from the paper in Section 9.

2. Observations

2.1. Photometry

Photometric observations were obtained by the ROTSE-IIIb telescope at McDonald Observatory (Akerlof et al. 2003). The ROTSE-III instruments are 0.45 m robotic Cassegrain telescopes with a $1\overset{\circ}{.}85 \times 1\overset{\circ}{.}85$ field of view (FOV). They operate with an unfiltered 2 k × 2 k pixel back-illuminated CCD with broad transmission over a wavelength range of 3000–10,000 Å achieving a typical limiting magnitude of ∼18 mag.

A sample of 12 SNe IIP is obtained from the ROTSE Supernova Survey comprised of three SN search programs spanning from 2004 to 2013. The ROTSE survey is not targeted to specific galaxies or SNe. The choice of fields was initially motivated by the need to cover local galaxy clusters in a search to discover new SNe. We do not impose any selection on host galaxy type or characteristics of any kind. The three phases of the ROTSE SN survey not only use the same telescope and detector but also exploit the same list of tiles with a few percent of additional tiles distinct in each phase. The data are reduced and analyzed with the same algorithms and pipelines for all three phases. A summary table of the 12 events with their host galaxies is given in Table 1. Each event in this sample has multiple photometric measurements between one and five weeks after explosion. We will discuss below why this time range is suited for the EPM technique using SNe IIP. This sample constituted four events from the Texas Supernova Search (TSS; Quimby 2006), five events from the ROTSE Supernova Verification Project (RSVP; Yuan 2010), and three events from the Texas Supernova Spectroscopic Survey (TS^3; Dhungana 2018). The TSS survey involved the northern sky survey using the ROTSE-IIIb telescope with nightly patrol of thousands of galaxies in the nearby clusters. The TSS aimed at amassing a small collection of well-observed SNe, targeting the earliest possible photometric observation, and likewise a triggered spectroscopic follow-up with the nearby Hobby Eberly Telescope (HET). The RSVP survey extended the northern sky with more fields using both the ROTSE- IIIb and IIId telescopes, along with the southern sky coverage using the IIIa and IIIc telescopes. The TS^3 survey continued with the RSVP fields in automated survey mode; however, new triggered follow-up photometric and spectroscopic observations were also added for the interesting events within and outside the existing ROTSE footprint. For most of the survey fields, the ROTSE observations are scheduled for paired successive one-minute exposure imaging 30 minutes apart. This scheduling is repeated 2–3 times separated by ∼2 hr. The follow-up auxiliary fields are generally scheduled using the same scheme, apart from a few interesting events where imaging cadence is increased. In the sample of 12 SNe IIP, 6 were discovered by the ROTSE telescopes, 5 others were observed in the regular survey mode, and 1 was observed in triggered auxiliary mode.

2.2. Spectroscopy

When available, spectroscopic observations were obtained by the Hobby Eberly Telescope (HET) at McDonald Observatory (Hill et al. 1998). The HET possesses a 9.2 m aperture with a 4′ FOV, using a 3072 × 1024 pixel CCD. The Low Resolution Spectrograph (LRS) is a high-throughput optical (∼4200–10,100 Å) grism spectrograph attached to the

Table 1
ROTSE IIP Sample for the EPM Study

SN	Program/ROTSE Field	Host Galaxy	Spectra	z	$E(B-V)_{\rm MW}$	$E(B-V)_{\rm tot}$	Adopted t_0(MJD)	BVI Photometry	References
SN 2004gy	TSS/skc1307 + 2626	NGP9 F379-0005009	1	0.02690 ± 0.00100	0.0100 ± 0.0007	0.0100 ± 0.0007	53362.5 ± 2.5	***N***	1
SN 2005ay	TSS/tss1152 + 4327	NGC 3938	3	0.00270 ± 0.00001	0.0183 ± 0.0002	0.0183 ± 0.0002	53452.5 ± 4.0	***N***	2,3
SN 2006bj	TSS/tss1220 + 0756	SDSS J122219.09 + 073725.5	1	0.03770 ± 0.00100	0.0200 ± 0.0004	0.220 ± 0.050	53815.3 ± 3.0	***N***	4
SN 2006bp	TSS/tss1159 + 5136	NGC 3953	4	0.00351 ± 0.00001	0.0260 ± 0.0060	0.4000 ± 0.0100	53833.7 ± 2.0	***N***	5,6
SN 2008bj	RSVP/sks1155 + 4643	MCG +08-22-20	1	0.01896 ± 0.00011	0.0230 ± 0.0010	0.0260 ± 0.1000	54534.0 ± 2.5	***N***	4
SN 2008gd	RSVP/sks0117 + 1352	SDSS J012044.48 + 144139.6	1	0.059096 ± 0.000053	0.0468 ± 0.0028	0.2823 ± 0.0582	54726.9 ± 3.5	***N***	4
SN 2008in	RSVP/tss1224 + 0440	NGC 4303	3	0.00522 ± 0.00001	0.019 ± 0.0002	0.1000 ± 0.1000	54825.1 ± 2.1	***Y***	6,7
SN 2009dd	RSVP/tss1209 + 4958	NGC 4088	3	0.00252 ± 0.00001	0.019 ± 0.0002	0.3670 ± 0.0070	54928.1 ± 1.3	***Y***	8,9
PTF10gva	RSVP/tss1225 + 1112	SDSS J122355.39 + 103448.9	1	0.02753 ± 0.00012	0.0263 ± 0.0008	0.0263 ± 0.0008	55320.3 ± 0.9	***N***	10
SN 2013ab	TS^3/vsp1443 + 0953	NGC 5669	2	0.00456 ± 0.00001	0.0234 ± 0.0002	0.044 ± 0.066	56339.5 ± 1.0	***Y***	11
SN 2013bu	TS^3/skt2237 + 3425	NGC 7331	1	0.002722 ± 0.000004	0.078 ± 0.0006	0.078 ± 0.0006	56399.3 ± 1.0	***Y***	1, 12
SN 2013ej	TS^3/rqa0137 + 1547	NGC 0628/M74	5	0.00219 ± 0.000003	0.0610 ± 0.0010	0.0610 ± 0.0010	56496.9 ± 0.3	***Y***	13

References. (1) Guillochon et al. 2017; (2) Gal-Yam et al. 2008; (3) Poznanski et al. 2010; (4) Kelly & Kirshner 2012; (5) Quimby et al. 2007; (6) Bose & Kumar 2014; (7) Roy et al. 2011; (8) Inserra et al. 2013; (9) Pejcha & Prieto 2015; (10) Khazov et al. 2016; (11) Bose et al. 2015; (12) Valenti et al. 2016; (13) Dhungana et al. 2016.

HET tracker, with resolving power of $R = \frac{\lambda}{\Delta\lambda}$ ranging from 600 to 3000.

Spectra for the SNe IIP sample that were obtained by the HET are archived in the WISeREP (Yaron & Gal-Yam 2012) catalog. For the events for which no HET spectrum is available, we obtain them from the literature, WISeREP or Open Supernova Catalog (Guillochon et al. 2017).

3. Data Reduction

3.1. Photometry

ROTSE III photometry is carried out using standard techniques (Yuan & Akerlof 2008; Dhungana et al. 2016). The online SN pipeline tasked with prompt analysis and SN discovery utilizes the image-differencing software developed for the RSVP (Yuan & Akerlof 2008). While this differencing is robust for the cases where the SN lies substantially out of the host core, we have sought to improve the detection efficiency and the root mean square (rms) scatter when the observation is photon limited or close to the host core. Therefore, we developed a new image-differencing software that we utilized in the offline ROTSE SN photometric data reduction pipeline.

3.1.1. Image-differencing Technique: Kernel Convolution

Image differencing is a common technique used to monitor and characterize the time domain variability of astronomical objects. Because of the variation of observational components across exposures, the exact nature of variability from the astrophysical source requires proper extraction by correctly modeling the backgrounds in each exposure and matching the point spread functions (PSFs). Precise measurements of variability have been performed using differencing technique in various circumstances (Alard & Lupton 1998; Bramich 2008; Kessler et al. 2015). We present a new differencing software for the ROTSE SN photometry analysis based on the kernel convolution technique (e.g., Alard & Lupton 1998; Becker et al. 2012). Due to the complexity of the bright background host with an extended PSF, the subtraction technique can yield photometric artifacts. ROTSE was designed to quickly image the large sky areas, thereby maximizing the sky coverage at the cost of spatial resolution. The pixel size of $\sim 1\farcs5$ is large on the scale of host galaxy morphology. It is also challenging to get an accurate measurement of the signal at the noise limit. Allowing a sufficiently large basis of PSF variation, this subtraction software, ImageDiff (Dhungana & Kehoe 2023), as developed on GitHub,[13] attempts to achieve better performance on the ROTSE image differencing, not only when the background is complicated but also when the signal is photon limited.

Given a recent survey(science) image $S(x, y)$, a higher signal-to-noise template image $T(x, y)$, usually prepared by stacking several past images, and a kernel basis $K(u,v)$, the survey image is modeled in a linear combination of kernel convoluted template as

$$S(x, y) = (K \otimes T)(x, y) + \epsilon(x, y). \quad (1)$$

Here, x, y are pixel coordinates, u, v are kernel coordinates, and $\epsilon(x, y)$ is the error term. The kernel basis set constitutes i basis kernels, i.e., $K(u, v) = \{k_i(u, v)\}$. We can write Equation (1) as a linear equation,

$$S = \sum_i A_i c_i + \epsilon, \quad (2)$$

where $A_i = k_i \otimes T$ and c_i are the coefficients for the linear combination. We intend to find these coefficients c_i corresponding to each kernel k_i. Assuming Gaussian errors, the maximum likelihood (minimum χ^2) solution for the coefficient matrix will be

$$C = (A^T N^{-1} A)^{-1} A^T N^{-1} S, \quad (3)$$

where N is the pixel noise matrix, which is a diagonal matrix, as the pixel errors are treated as statistically uncorrelated. The inverse of the covariance matrix $A^T N^{-1} A$ must exist. A small prior is added at the level of machine precision, to ensure the matrix remains well conditioned.

The residual image after subtraction of the background (hereafter difference image) is then simply given in pixel coordinates by

$$D(x, y) = S(x, y) - \left(\sum_i A_i c_i\right)(x, y). \quad (4)$$

3.1.2. Kernel Types

We use four different kernel bases, defined as follows.

1. Sum of Gaussians basis: Gaussian functions multiplied by two-dimensional polynomials

$$k_i(u, v) = e^{-(u^2+v^2)/2\sigma_n^2} u^p v^q, \quad (5)$$

where i runs over all permutations of n, p, q. The polynomial order expansion used is $0 \leqslant p + q \leqslant O_n$. The default choices for three Gaussians are $\sigma = [0.7, 1.5, 3.]$ with $O_n = [4, 3, 2]$. The resulting total number of kernels $= \sum_n (O_n + 1) \times (O_n + 2)/2 = 31$.
2. Gauss–Hermite polynomial basis: A Gaussian core is multiplied by Hermite polynomials, giving

$$k_i(u, v) = e^{-(u^2+v^2)/2\sigma^2} H_m(u) H_n(v), \quad (6)$$

where $H_n(x) = (-1)^n e^{x^2} \frac{d^n}{dx^n} e^{-x^2}$ is the nth-order Hermite polynomial. An obvious merit of using the Gauss–Hermite kernels over symmetric Gaussian kernels is that the former can model asymmetry because of the odd–even nature of the Hermite polynomials. An asymmetric PSF can occur for many different reasons, such as atmospheric conditions.
3. Delta function basis: This kernel constitutes only delta functions,

$$k_{i,j}(u, v) = \delta(u - i)\delta(v - j). \quad (7)$$

An 11×11 pixel size kernel has 121 orthonormal, single-pixel bases. The benefit of the delta function is that it is independent of shape, so there is no parameter to tune. However, this may need regularization to ascertain proper conditioning of the model in order to prevent from overfitting. See Becker et al. (2012) for an application of delta function kernels.
4. Principal Component Analysis basis: We have also adopted a principal component analysis (PCA)-based image differencing. PCA is a technique of reducing data dimensionality without losing any significant feature of

[13] https://github.com/rotsehub/ImageDiff/releases/tag/23v1.0

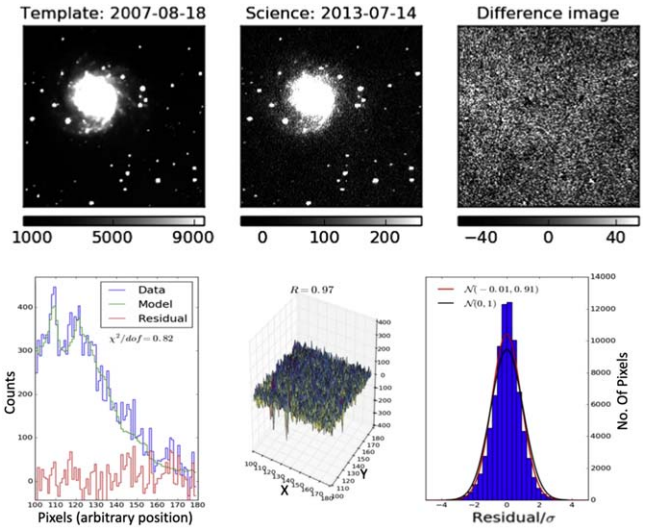

Figure 1. Top: A high-S/N template subimage (left) and a survey subimage (middle) of the ROTSE-IIIb field rqa0137 + 1547, and the difference image using `ImageDiff` (right). Bottom: A slice from the center of the subimage showing the galaxy *M*74 profile, the fit model and the residual (left). For clarity, the same residual in 2D shown in 80 × 80 pixels (middle), where R is the measure of the fraction of observation variance preserved in the difference image. In the right panel, a pull distribution shows a Gaussian fit (red) yielding a residual $\mathcal{N}(-0.01, 0.91)$ and the theoretical zero mean, unit variance standard normal distribution (black). The pull is close to the standard normal distribution.

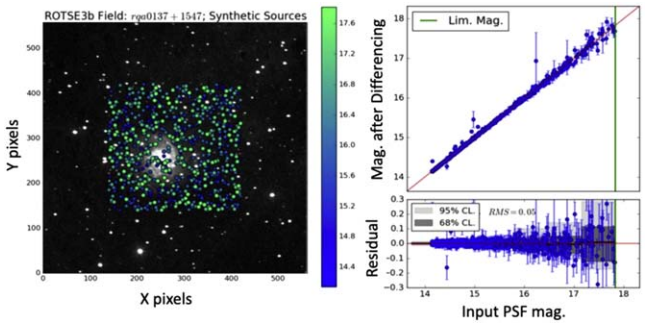

Figure 2. Left: 1000 simulated sources superimposed on a data image. Points show injected sources but do not represent the true PSF shape of the simulated objects. Right: Performance of `ImageDiff`. Overall residual mean is 0, yielding no bias, with an rms ∼0.05 magnitude; although close to the limiting magnitude, the rms is ∼0.1 mag. The pull distribution is $\sim\mathcal{N}(0.1,\ 0.94)$.

Table 2
χ^2 and *R* Values of Differencing Using Different Kernels for ROTSE Field rqa0137 + 1547 (Figure 1)

Kernel Type	χ^2/dof	*R* Value	Pull
Gaussian sum	0.82	0.97	$\mathcal{N}(-0.01, 0.91)$
Gauss–Hermite	0.82	0.97	$\mathcal{N}(-0.01, 0.90)$
Delta Function	0.81	0.97	$\mathcal{N}(-0.01, 0.90)$
EMPCA	0.85	0.93	$\mathcal{N}(0.03, 0.94)$

the data. The principal components are the eigenvectors of the covariance of the data set. They are sorted by the eigenvalues in decending order, i.e., along the component with the highest eigenvalue (first component), the variance is maximized. From the kernel-convolved templates using one of the kernels above, we construct an orthogonal eigen-basis using PCA. In this case, the basis set is transformed from image space to PCA space. We use the `empca` package (Bailey 2012) to compute the PCA using the expectation maximization (EM) method.

The top panel of Figure 1 shows a high-S/N template image, a later survey image, and the output difference image for a subimage of ROTSE SN field rqa0137 + 1547. The bottom panel shows a slice of the galaxy profile, the model PSF using the sum of Gaussian kernels, and the residual from the subtraction. The rightmost plot shows the Pull distribution for the residuals in normal form ($\mathcal{N}$), defined as

$$\text{Pull} = \sum_i \frac{\text{data}_i - \text{model}_i}{\sigma_i}, \tag{8}$$

where *i* runs over all the pixels in the subimage. A performance summary of the image-differencing algorithm using different kernel types on the same field survey image is shown in Table 2. We also perform image differencing on other ROTSE fields and observe no significant variation in the choice of kernels other than the delta function, which required adjustments of the regularization parameter. Therefore, we use sum of Gaussian kernel basis for all our IIP SNe to obtain the final photometry for this analysis.

3.1.3. Performance of Image Differencing

We monitor the performance of the differencing algorithm for both the spatial and temporal PSF variation in the following two ways. We simulate the PSF in order to establish the proper performance of the template subtraction, and we consider lightcurve properties to comment on the efficiency and stability of the source photometry. We consider the former using a PSF model profile with a Gaussian core and a wing component, allowing ellipticity variation from Bolton & Schlegel (2010):

$$I(x, y) = \frac{(1-b)}{\sqrt{2\pi}\,\sigma} e^{\left[\frac{-r_{\rm ell}^2}{2\sigma^2}\right]} + \frac{b e^{(-r/r_0)}}{2\pi r r_0} \tag{9}$$

$$r_{\rm ell} = \sqrt{qx^2 + y^2/q}\,, \tag{10}$$

where *b* controls the wing contribution, *r* is the radial offset from the PSF center, r_0 is the characteristic size of the wing, *q* is the ellipticity, and *x* and *y* are related to CCD coordinates by rotation/translation. Monte Carlo (MC) simulation is performed by injecting objects of random magnitudes at random locations within a subimage of a ROTSE survey image. To disallow tight blending of the injected source with the point data sources in the image, a `scikit` (Pedregosa et al. 2011) $k-d$ tree query is performed taking a radius of 1 FWHM of the PSFs of the data image, derived by `sextractor` (Bertin & Arnouts 1996). For the injected sources, the image subtraction is performed iteratively one by one, and the final photometry is performed on the difference image. The extracted magnitudes are compared with the input magnitudes. An example simulation for the ROTSE field *rqa* 0137 + 1546 is shown in Figure 2. The rms of the photometry residuals is at the 0.05 magnitude level, and a pull distribution shows a normal $\sim\mathcal{N}(0.1,\ 0.94)$ distribution.

In most of the SNe analyzed, the new image subtraction yields 10%–20% more detections, and the scatter of the residuals also is remarkably narrower. The top panel of Figure 3 shows an example of image differencing of an epoch of SN 2004gk using the new image-subtraction software. The

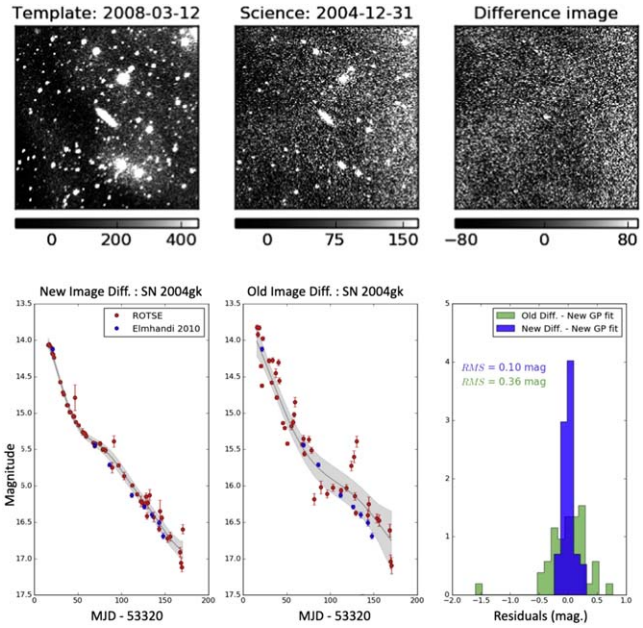

Figure 3. Top: Image subtraction of a 280 × 280 pixel subimage of ROTSE tss1246 + 1249 field: a high-S/N template image (left) obtained with stacking 30 past images, a survey image with potential SN at the center (middle), and the difference image from `ImageDiff` using the sum of the Gaussian kernel convolutions of the template image. SN 2004gk is clearly visible at the center of the difference image. Bottom: Photometric performance using new and old image-differencing methods for SN 2004gk. The reduced data points are normalized to the Elmhamdi et al. (2011) *V*-band magnitude (shown in blue points) on MJD 53389.0, to train the eye. The solid line is a Gaussian process regression fit, with the filled region being the 95% confidence posterior prediction. The rightmost panel shows the residuals of old (green) and new (blue) lightcurves after subtracting the respective best fits. The rms scatters for the green and blue histograms respectively are 0.36 and 0.10 mag, and the pulls on the new image differencing yield a dispersion of 1.03, which is substantially improved compared to the old differencing, where the pull yields a dispersion of 2.82.

SN is clearly observed in the residual image on the right. The bottom panel shows the lightcurve of SN2004gk obtained using the old and new image subtraction. Each lightcurve is fitted with Gaussian Process (GP) regression using `scikit`. The rightmost plot shows the residuals of new and old lightcurves obtained after subtracting the GP best-fit models. It can be observed that the new image differencing not only has higher detection efficiency but also improves the scatter of the residuals by a factor of 3.5. The pull distributions are found to be $\mathcal{N}(0.01,\ 1.03)$ for the new and $\mathcal{N}(0.39,\ 2.82)$ for the old method, suggesting no significant bias due to the new method. The typical pulls on the other SN lightcurves obtained with `ImageDiff` also follow within 10% of a standard normal distribution $\mathcal{N}(0,\ 1)$.

3.1.4. Photometric Calibration

ROTSE magnitudes are calibrated to magnitudes from the APASS[14] DR9 catalog. These ROTSE magnitudes are corrected for the available total extinction. When no total extinction is available, we still correct for Milky Way extinction using the color excess $E(B-V)_{\rm MW}$ from the Schlafly & Finkbeiner (2011) model. We perform the photometric extinction correction for the obtained $E(B-V)$ values using the A_λ/A_V ratio given in Table 3 of Cardelli et al. (1989). It should be noted that the ROTSE CCD response is significantly different from the *V*-band filter response function. To establish a concrete and accurate calibration for the rapidly evolving Spectral Energy Distribution (SED) of SNe IIP, we quantify any potential offset associated with the calibration of ROTSE flux with the *V*-band flux of the field stars. We perform Monte Carlo simulations of blackbody continuum spectra of varying temperature 2–17 kK, randomly normalized to the *V*-band magnitude in the range 12–18. The selection of temperature range (Section 5.3) and magnitude range agrees with the observed SN IIP temperatures and magnitudes for epochs similar to those in the sample. The blackbody spectra are convolved with the ROTSE response function and the *V*-band filter response function, and magnitudes are estimated. The left plot of Figure 4 shows the comparision of the simulated magnitudes for the ROTSE and *V* band. It is clear from the scatter that there is need for correction in both directions. To address these offsets, we use an exponentially growing function of temperature (T):

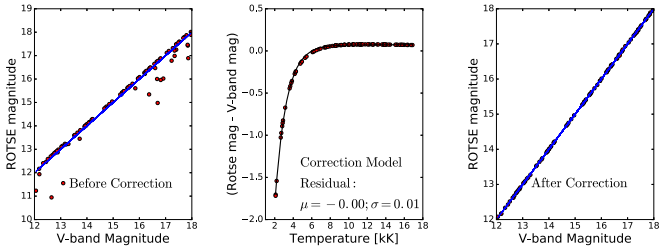

Figure 4. Correction of systematic effects of calibrating ROTSE magnitudes to catalog *V*-band data. Shown are the offsets in scatter plot for 100 Monte Carlo blackbody spectra spanning temperatures of 2000–17,000 K, randomly normalized to a *V*-band mag range 12–18 (left), with offsets varying with temperature and the correction model given by Equation (11) (middle) and offsets after applying correction (right).

$$m_{\rm ROTSE},\ V - V = a + b(1 - e^{cT}) \equiv \text{corr}, \qquad (11)$$

where $m_{\rm ROTSE,V}$ is the magnitude obtained from calibrating to *V* data before correction. The final calibrated magnitude is then $m_{\rm ROTSE},\ V - \text{corr}$. Best-fit model parameters obtained using the simulation of 100 random blackbody spectra yield $a = -9.46 \pm 0.11; b = 9.52 \pm 0.11$ and $c = (8.06 \pm 0.048) \times 10^{-4}$. The state before correction, the correction model, and the magnitudes after applying the correction for the 100 Monte Carlo sample are shown in the middle and the right plot of Figure 4. The rms in the residuals is about 0.01 mag, and no fundamental bias is observed from the correction. The residual rms is much smaller than the typical statistical uncertainty of the obtained ROTSE magnitudes, and it is propagated as uncorrelated systematic uncertainty in the final photometry. As broadband observations are not available for the events in the sample at all epochs, and we are explicitly measuring and modeling temperature evolution in Section 5, we used a temperature-dependent correction model. A color-dependent correction would require broadband observations at the photometric epochs. When compared with the available *V*-band data of several IIP SNe in the sample, the corrected photometric measurements during the plateau phase are found to be statistically consistent.

[14] https://www.aavso.org/apass

3.2. Spectroscopy

HET data are reduced using standard spectroscopic techniques as described in (Silverman et al. 2012; Dhungana et al. 2016). Other spectra are obtained in the fully reduced form from the literature or from databases. We first correct for the MW reddening using the Fitzpatrick (1999) model. Then we convert all the spectra to the SN rest frame. For the samples where we have obtained host extinction, we further correct for reddening due to the host using the Fitzpatrick (1999) model.

3.3. Extinction, Redshift, and Explosion Epochs

Table 1 provides our adopted total extinction, the redshift, and the explosion epochs for each event in our sample. We refer to the literature for respective measurements. When no extinction is available for the host, we adopt MW extinction only using Schlafly & Finkbeiner (2011). Because the host contributions are not available for all events, we suggest that readers use their estimated values for the host extinction. When the explosion epochs are not available, we adopt the arithmetic mean of the first detection and latest nondetection in the ROTSE photometry or such reported in the literature, whichever provides the best constraint. For our sample, explosion epochs have uncertainties of 0.3–4 days. The redshifts are taken from the literature or the galactic redshift from the NED[15] database, unless otherwise noted.

3.4. K-Correction

Because we do not have color information from broadband photometry for all the events in our sample, we perform a spectrophotometric approach to obtain the K-correction for events with $z > 0.01$. First, to determine the K-correction for each event, the spectroscopic data of all the nearby SNe ($z < 0.01$) samples during the plateau phase are redshifted by the value for the SN considered, and both the observer frame and the SN rest frame magnitudes are taken by applying the V-band filter. The difference of the rest frame magnitudes from the observer frame gives the K-correction for the respective spectroscopic epochs. Once the K-corrections are obtained from the sample at the spectroscopic epochs, they are also evaluated for the spectra of the SN for which the K-correction is to be determined. A temporal Gaussian Process (GP) regression is performed on the obtained K- correction values to make a prediction of K- correction for the desired photometric epochs of each SN with $z > 0.01$. An example GP regression fit and the 68% confidence level posterior prediction are shown in Figure 5 for SN 2004gy (top) and SN 2008bj (bottom). We propagate the uncertainty from K-correction as systematic uncertainty in the final photometry and later analyses.

The final, fully reduced lightcurves for the ROTSE IIP SN sample, after calibration to APASS V magnitude and SED, and corrected for extinction and K-correction (for $z > 0.01$), are shown in Figure 6.

4. Expanding Photosphere Method and Observables

With the advent of more sensitive, deeper surveys, SNe IIP discovery is increasing. While competitive samples to perform precise cosmological studies at the higher redshifts are still

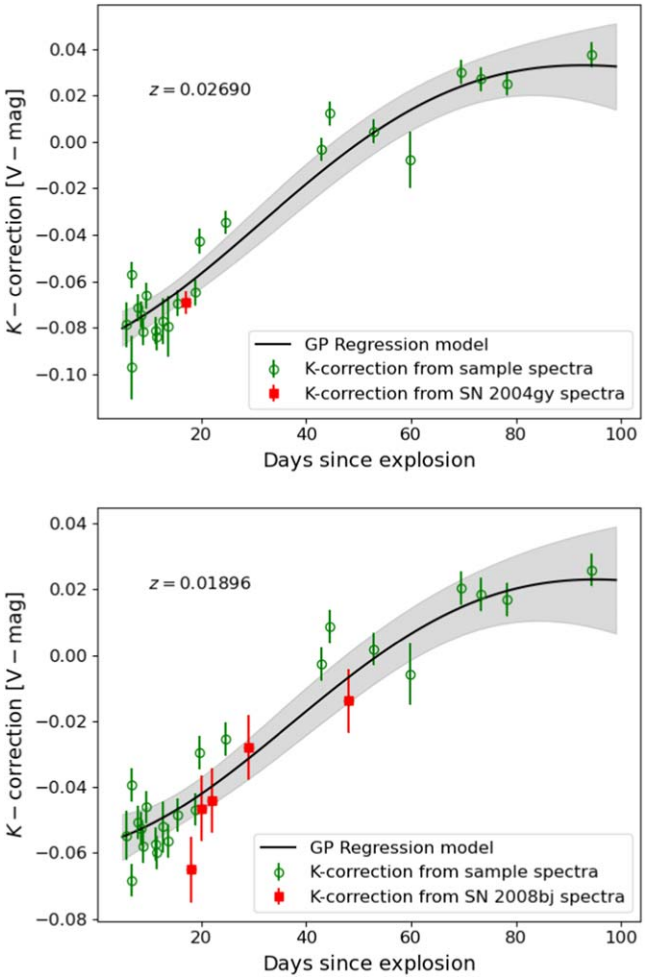

Figure 5. Top: K-corrections derived spectroscopically from the $z < 0.01$ SNe sample (green circles) and the SN2004gy spectrum (red squares) for $z = 0.02690$, corresponding to SN 2004gy. The solid line is the best-fit GP model, and the shaded region represents the 68% confidence region for the posterior. Bottom: The same as the top, but for $z = 0.01896$, corresponding to SN 2008bj.

accumulating, improvements in calibration for distance estimates have been explored using both photometry and spectroscopy in the lower-redshift domain. We utilize the Expanding Photosphere Method (EPM) to estimate distances of our SNe IIP sample. We follow the prescription of Dhungana et al. (2016) and Dhungana (2018) to describe the fundamental EPM equation, given by

$$t = D \times \left(\frac{\theta}{v_{\rm phot}}\right) + t_0, \tag{12}$$

where t represents the observing time, D is the distance to the SN, $\theta = 2R/D$ is the angular size of the photosphere at t, $v_{\rm phot}$ is the expansion velocity of the photosphere at t, and t_0 is the moment of the shock breakout.

Assuming isotropic radiation from a blackbody, the observed flux can be written as

$$f_\lambda^{\rm obs} = \theta^2 \pi B_\lambda(T) 10^{-0.4A_\lambda}, \tag{13}$$

where $B_\lambda(T)$ is the Planck function for the blackbody of effective temperature T. Here, A is the galactic extinction for

[15] https://ned.ipac.caltech.edu/

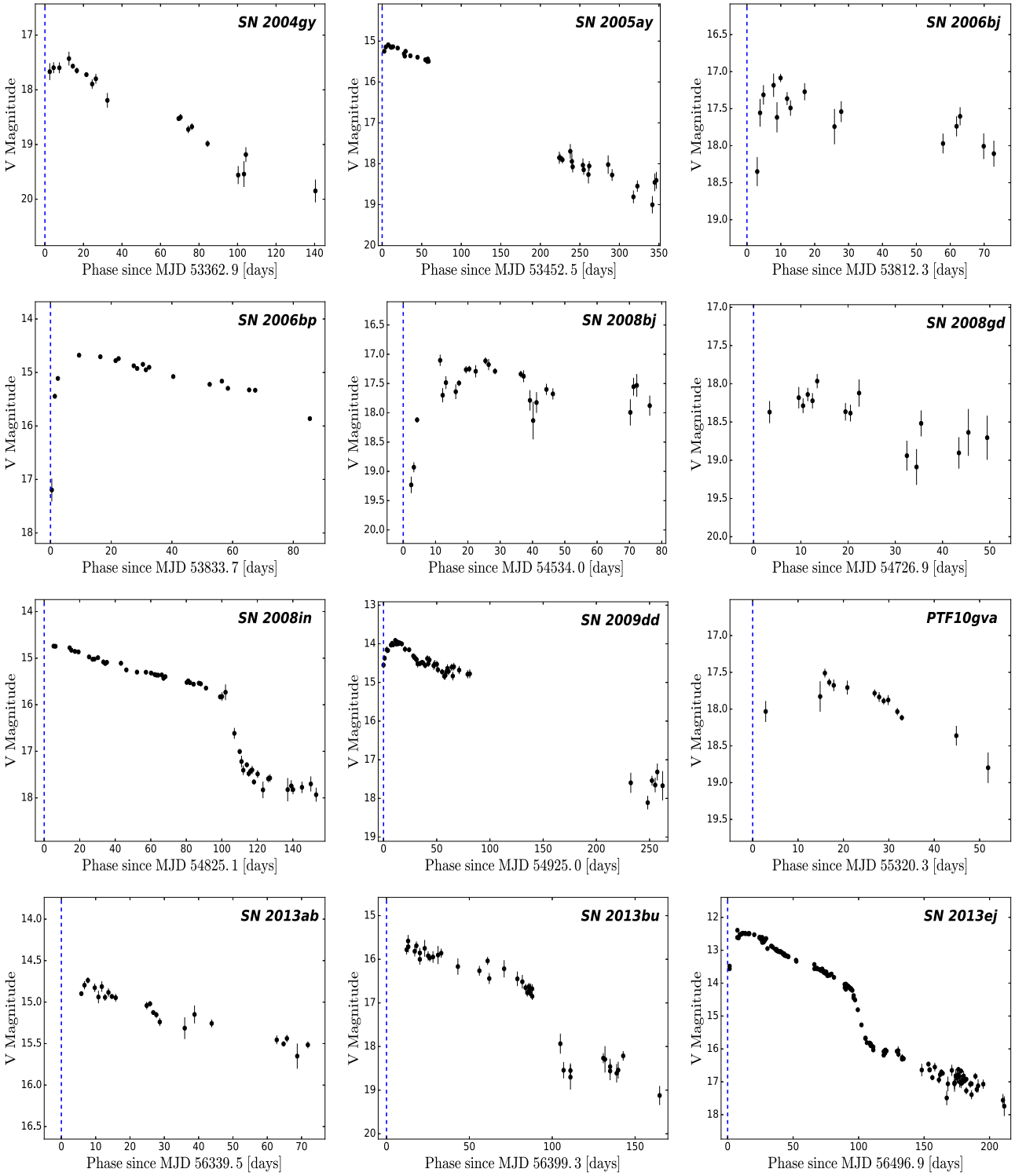

Figure 6. Lightcurves of SNe in the ROTSE IIP sample after final photometric reduction and calibration. The ROTSE magnitudes are calibrated to APASS V band, followed by the SED correction using Equation (11) and the extinction correction. SNe with $z > 0.01$ also include an additional K-correction. A blue dashed line in each plot represents the adopted explosion epoch for that respective event.

the observed photometric band. The subscript λ should be taken as an index for the observed photometric bands. Unlike a perfect blackbody, where the thermal photons emerge from the photosphere, the surface of last scattering (e.g., Jones et al. 2009; Bose & Kumar 2014), SNe IIP photons are generated from the deeper atmosphere. Therefore, the parameter θ in Equation (12) corresponds to the thermalization layer, while $v_{\rm phot}$ in Equation (12) corresponds to the photosphere (optical depth, $\tau = 2/3$), and the atmosphere is considered gray (e.g., Eastman et al. 1996; Jones et al. 2009). A scaling factor ζ, also termed the dilution factor or distance correction factor, is introduced as the ratio of the radius of the thermalization layer

to that of the photosphere:

$$\zeta = \frac{R_{\rm therm}}{R_{\rm phot}}. \quad (14)$$

Commonly, ζ is treated as a wavelength-independent parameter in the optical and infrared regime as described by Eastman et al. (1996), who also show that it is a monotonic function of T for several weeks after the explosion. Thus, to exploit EPM on SNe, care should be taken to select the measurement epochs when the wavelength dependence is not very significant. Complex computation of a realistic model atmosphere is required to accurately estimate ζ, and that is beyond the scope of this paper. We employ the commonly used prescription of Dessart & Hillier (2005), and include ζ_λ in Equation (13):

$$f_\lambda^{\rm obs} = \zeta_\lambda(T)^2\theta^2\pi B_\lambda(T)10^{-0.4A_\lambda}. \quad (15)$$

Ideally, one could consider full extinction-corrected bolometric flux by integrating over all the wavelengths. With the bolometric flux, θ can be obtained with

$$\theta = \frac{1}{\zeta(T)}\sqrt{\frac{f_{\rm bol}}{\sigma T_{\rm eff}^4}}, \quad (16)$$

where σ is the Stefan–Boltzmann constant. However, direct measurements of bolometric flux are not obtained in practice. Photometry is performed using specific passbands. Thus, the filter response function is always convolved with the native flux from an SN, giving its magnitude in that wave band. Many SNe in the ROTSE IIP sample lack observations to yield or calibrate to the full bolometric flux. Therefore, we derive the effective blackbody flux by convolving with the filter response function $R_\lambda(\lambda)$, i.e.,

$$b_\lambda(T) = \int_0^\infty R_\lambda(\lambda')\pi B(\lambda', T)d\lambda'. \quad (17)$$

Therefore, with the observed flux in a given passband λ and for the given value of $\zeta_\lambda(T)$, θ can be obtained using

$$f_\lambda^{\rm obs} = \zeta_\lambda(T)^2\theta^2 b_\lambda(T)10^{-0.4A_\lambda}. \quad (18)$$

The observed fluxes here should be treated as the K-corrected flux, whereas the parameters ζ_λ and b_λ are in the SN rest frame. K-correction accounts for the $(1+z)$ factors that would appear in the equations for high-redshift SNe. Thus, the derived distance will be the luminosity distance and not the angular diameter distance. We refer readers to Gall et al. (2016) and references therein for further discussion. The distance can be estimated using Equation (12) by determining $v_{\rm phot}$ and T, which can be directly obtained from observations. Then, both the parameters D and t_0 can be simultaneously obtained by minimizing the χ^2 using

$$\chi^2 = \sum_j \frac{\left[\frac{\theta_j}{v_{{\rm phot}_j}} - \frac{(t_j - t_0)}{D}\right]^2}{{\sigma_j}^2}, \quad (19)$$

where σ_j is the uncertainty on $\theta_j/v_{{\rm phot}_j}$.

5. SNe IIP Properties

The EPM distance estimation from Equation (19) now requires for each event a sample of $v_{\rm phot}$ and θ measurements. While $v_{\rm phot}$ at any epoch can be estimated from the line profiles in a spectrum, θ is obtained through temperature estimation and comparision with the concurrently observed photometric flux using Equation (15). In practice, however, both the spectroscopic and photometric measurements do not occur concurrently. Based on the available data, we will establish below the interpolation/extrapolation models to estimate the parameters at the desired epochs.

5.1. Explosion Epoch

Whenever available, the moment of explosion (t_0) for each of the IIP SNe sample is adopted from the literature as noted in Section 3.3. When no estimate is available, we take t_0 to be the midpoint of the first of the ROTSE or a publicly available photometric detection, and the most recent prediscovery nondetection epoch in the ROTSE data. We propagate the difference of t_0 and the prediscovery epoch to the systematic uncertainty in t_0. Both the adopted explosion epoch and the respective uncertainty are given in Table 1.

5.2. Photospheric Velocity

As the SN IIP ejecta exhibit an extensive H-envelope during early times, the photospheric velocities are generally estimated directly from the weak line signatures such as those of Fe II lines. While in the plateau phase, the absorption minima of the P Cygni profiles of Fe II λ4924, λ5018, and λ5169 have been used as the best estimators of the photospheric velocity (e.g., Leonard et al. 2002; Dessart & Hillier 2005; Nugent et al. 2006), in the earlier epochs these lines cannot be observed. When observed, we strictly use Fe II λ5169 velocity measurements for the $v_{\rm phot}$. When Fe II λ5169 is not observerd at early times, we use the He II λ5876 line. On rare occasions, when He II lines also are not observed, we use correlations of the H Balmer line velocity with the Fe II line velocity from Faran et al. (2014) to obtain an effective $v_{\rm phot}$.

5.2.1. Measurement

A convenient way to estimate the position of the line minimum is to perform a Gaussian fit of the absorption profile. Accurate measurements are complicated by typically blended features and continuum subtraction. We perform a 1D Gaussian mixture modeling (GMM) of a segment of the spectrum around each line of interest. We define a signal region considering the whole line profile. We consider a few hundred Angstroms on both sides of the signal region as the side bins and a continuum is estimated by performing a spline fit on the side bins. GMM is performed iteratively on the continuum-subtracted absorption profile. The best-fit GMM model gives the optimum number of the Gaussian components as the maximum likelihood fit of this absorption profile. We measure the Bayesian Information Criterion (BIC) and Akaike Information Criterion (AIC) for each model as we increase the number of components for each iteration. The model that yields the minimum BIC from the GMM fit is chosen to be the best model. We also monitor the AIC to ensure that it does not severely contradict with the best model from the minimum BIC value. The position of the component aligned with the line of interest will give the best-fit value and the uncertainty of the photospheric velocity. An example involving this process of estimating line velocity for the Hβ line taking a spectrum for SN 2004gy from Jan. 10, 2005 is shown in Figure 7. The top left panel shows the

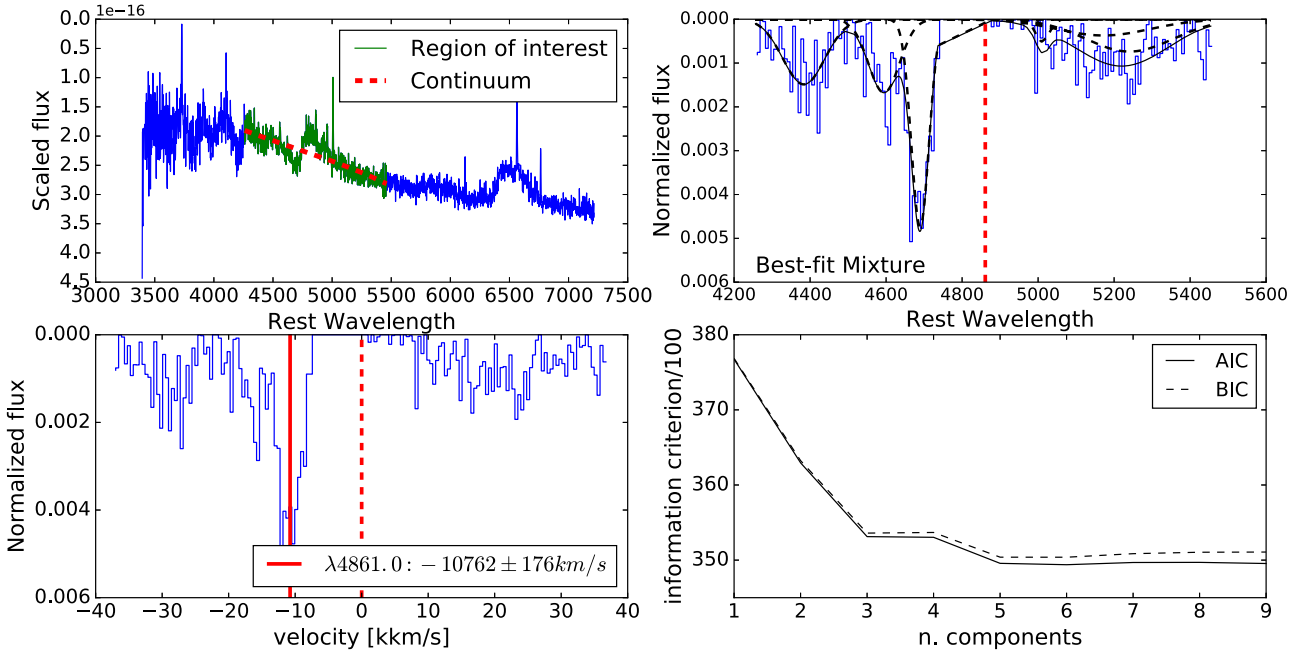

Figure 7. Estimation of the velocity of the Hβ line using the GMM model. Top Left: A spectrum of SN 2004gy taken on Jan 10, 2005. The continuum is estimated using a spline fit on the side bins around the signal region of 4500–5000 Å. Top Right: The normalized residuals on the continuum-subtracted absorption profile. The best-fit mixture model is shown in solid black, and the respective six Gaussian components are shown in dashed black lines. The dashed vertical line is the rest frame line position for Hβ. Bottom Left: Estimation of the line velocity from the best fit. The dashed vertical line indicates the rest frame position of Hβ, and the solid line shows the position of the absorption minimum obtained from the best fit. Bottom Right: BIC and AIC estimation for the mixture model with the multiple number of Gaussian components (n) performed iteratively for $n = 0$–9. The best fit has the minimum BIC and corresponds to $n = 6$.

estimation of the continuum obtained from the spline fit performed on the side bins around the signal region of 4500–5000 Å. Shown in the top right are the normalized residuals on the absorption profile after subtracting the continuum. GMM is performed iteratively by varying the number of components from 0–9. The bottom right panel shows the corresponding BIC and AIC values for each mixture model. The best-fit model with the minimum BIC has six Gaussian components, and the corresponding model and the Gaussian components are shown on the top right panel. The line velocity is obtained from the minimum of the Gaussian component corresponding to Hβ and is estimated to be 10760 ± 176 km s^{-1}, shown in the bottom left panel.

5.2.2. Extrapolation Model

Once the ionic velocities are measured directly from the GMM on the observed spectra, we want to interpolate/extrapolate these measurements to the photometric observation epochs. Previous studies such as Poznanski et al. (2010) and Faran et al. (2014) have empirically modeled the temporal evolution of prominent ionic signatures such as from Fe II lines. While Fe II lines tend to track the photospheric velocity, these lines are generally unobserved during the first few weeks. We show below that extrapolating such a model to early times shows a steeper decline than the velocities directly observed from He II lines.

We assemble the line velocities of three well-sampled supernovae from the literature and observe the time series evolution of the $v_{\rm phot}$. We first test an exponentially decaying model that appears to closely capture the $v_{\rm phot}$ evolution for each event during the epochs considered. Furthermore, when the epochs and $v_{\rm phot}$ of each SNe are calibrated relative to 50 days values, and the exponential model is fitted on the full distribution, we observe the rms scatter to decrease significantly, yielding a reasonable χ^2/dof of 0.60 for the fit. We note that the choice of 50d has been commonly made in the literature, and for SNe IIP, this is about midpoint of the typical plateau phase where the evolution is relatively smooth. We use an exponentially decaying model for the velocity evolution, given by

$$\frac{v_{\rm phot}(t)}{v_{\rm phot}(50)} = a + b\,\exp[-c \cdot (t/50)]. \quad (20)$$

The best-fit parameters for the velocity evolution in Equation (20) are estimated to be $a = 0.735 \pm 0.025$, $b = 2.650 \pm 0.064$, and $c = 2.327 \pm 0.589$. The left panel of Figure 8 shows the time evolution of the $v_{\rm phot}$ for three SNe obtained from the GMM fit of the absorption profile of ions during the photospheric period. The middle left plot shows our best-fit model after calibrating relative to 50 days. The middle right plot shows the residuals for different models after subtracting the $v_{\rm phot}$ evolution best-fit model shown in the middle left panel. The blue line is the residual for velocity model, obtained using only Fe II lines extrapolated in the earlier times, after subtracting the best-fit $v_{\rm phot}$ model. Also shown in red is the residual for the Fe II evolution model from Faran et al. (2014), extrapolated at early times, after subtracting the same best-fit model. For comparison, all three models are anchored at $v_{\rm phot}(50) = 4000$ km s^{-1}, and the respective shaded regions indicate their 68% confidence regions. We see the Fe II only model yields a steeper velocity evolution than the $v_{\rm phot}$ model using He II lines at early times.

To estimate the $v_{\rm phot}$ for our IIP sample, we first measure line velocities directly from the obtained spectra of the respective SNe. We apply the $v_{\rm phot}$ evolution model Equation (20) to

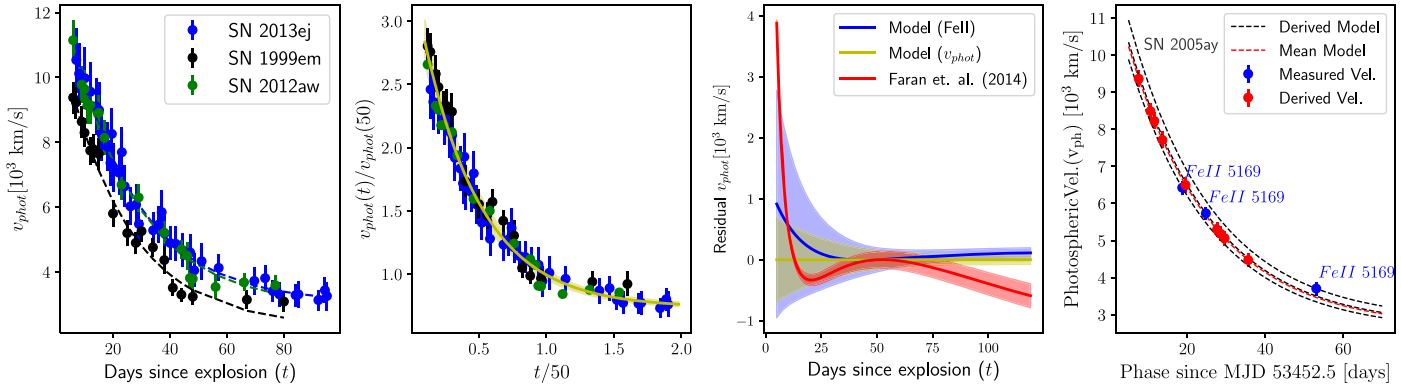

Figure 8. Left: Measured photospheric velocities and the evolution for three well-studied SNe IIP. Each velocity is derived from fitting relevant spectral lines using the GMM model from the spectra at corresponding epochs. The color-coded dashed lines represent the exponential decay-law fits using Equation (20) for the respective events. Middle Left: The global decay-law fit after calibrating the epochs and $v_{\rm phot}$ relative to 50 day values for each of the SNe. The best-fit model, shown with the solid line, has a $\chi^2/{\rm dof} = 0.60$. Middle Right: The residual velocity evolution models after subtracting the best-fit $v_{\rm phot}$ model shown in the middle left panel. The residual obtained for model obtained using Fe II lines alone is shown in blue, and the red line is the residual obtained for the Fe II model evolution from Faran et al. (2014). All three are shown relative to an arbitrary pivot point of $v_{\rm phot}(50) = 4000$ km s^{-1}. Right: Measured and derived $v_{\rm phot}$ models for SN 2005ay using the best-fit model. The blue points are the labeled ion velocities measured directly from the spectra using GMM. The black dashed curves are the respective $v_{\rm phot}$ models calibrated to the three blue points. The red dashed curve is the model calibrated to the weighted mean velocity $v_{\rm phot}(50)$, and red points are the derived estimates at the SN photometric epochs.

obtain the $v_{\rm phot}(50)$, and use it as anchor to sample the velocities at the desired photometric epochs. For events with multiple spectra, a weighted mean of $v_{\rm phot}(50)$ is obtained, and the $v_{\rm phot}$ at the photometric epochs are obtained anchoring the model (Equation (20)) using this average $v_{\rm phot}(50)$. We propagate the statistical error as uncorrelated systematic uncertainty from $v_{\rm phot}$ into the distance error budget for each SN. An example showing the directly estimated $v_{\rm phot}$ and the evolution model for the SN 2005ay is shown in the rightmost plot of Figure 8. The blue points are the measured velocities for the labeled ions. The black dashed curves represent the respective models pivoted at the measurement epochs, while the red dashed curve is the model anchored at the average $v_{\rm phot}(50)$ measurement, and red points are the velocity estimates at the photometric epochs of the SN. We perform the same procedure for all 12 events in our SNe IIP sample. We propagate the uncertainty on $v_{\rm phot}$ due to the evolution model as a 100% correlated uncertainty across all 12 SNe in the sample.

5.3. Temperature

The parameter θ in Equation (19) is obtained by comparing the observed flux from the SN with the effective blackbody flux after accounting for the dilution correction as shown in Equation (15). To determine the effective blackbody flux, we would like to estimate the temperature from fitting the SED constructed from the *BVI* phototmetric measurements to a Planck function.

5.3.1. Measurement

To estimate the effective color or blackbody temperature, we take the spectra for each event and spectrophotometrically determine the *BVI* fluxes from each of them. For each event, we use the reddening-corrected rest-frame spectra obtained from the procedure described in Section 3.2. Further, we derive a set of synthetic *BVI* magnitudes at the rest frame convolving with the respective filter response function, and the resulting SED is fitted to a Planck function to estimate the effective temperature as before. For cases where the spectral coverage is not wide enough to synthesize the *BVI* fluxes, the corrected spectrum is fitted directly to the Planck function after masking the Hα line and the telluric lines from the atmosphere when present. For a few events where simultaneous *BVI* photometry could also be obtained from the literature as shown in Table 1, we fit the measured rest-frame SED to a Planck function directly, and temperature is obtained as a fit parameter. At matching epochs, we found these estimates to be consistent with those derived spectrophotometrically.

5.3.2. Extrapolation Model

To estimate the temperature at the ROTSE photometric epochs, we first empirically establish an analytic relation of the temperature evolution using a sample of very well-observed SNe IIP. As shown in the left panel of Figure 9, an exponentially decaying model appears to accurately capture the temperature evolution for each event during the epochs considered. We pursue an approach to generate our temperature evolution model analogously to the velocity evolution model described in Section 5.2.2. We translate the epochs and temperatures of each SNe relative to the 50 day values and perform an exponentially decaying model fit on all three SNe. We observe the rms scatter to decrease significantly as shown in the middle panel of Figure 9. The choice of a 50 day epoch is consistent with the velocity evolution model. The exponential model for the temperature evolution is given by

$$\frac{T(t)}{T(50)} = a + b\,\exp[-c\cdot(t/50)]. \quad (21)$$

The best-fit model for the full sample yields $a = 0.908 \pm 0.012$, $b = 2.662 \pm 0.091$, and $c = 3.492 \pm 0.143$, as shown in Figure 9, and yields a $\chi^2/{\rm dof} = 1.04$. We also note that a power-law model with decay index of -0.44 ± 0.01 also yields a reasonable estimate with a $\chi^2/{\rm dof} = 1.6$. The adopted exponential model serves to reproduce the full temperature evolution if one temperature is measured at any epoch. The temperature estimated directly from the *BVI* fluxes is used to estimate $T(50)$ using Equation (21). Similar to the photospheric

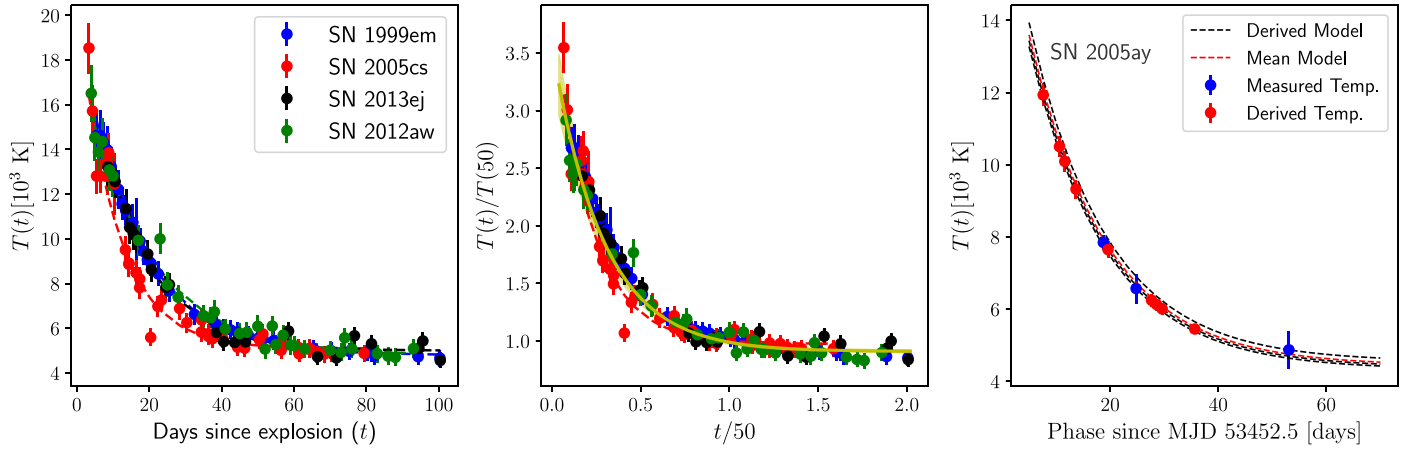

Figure 9. Left: Measured color temperature and the evolution model for four well-studied SNe IIP. Each temperature is derived from fitting *BVI* fluxes to a Planck function. The color-coded dashed lines represent the exponential decay-law fits using Equation (21) for the respective events. Middle: The global decay-law fit after calibrating the epochs and temperature relative to 50 day values for each of the SNe. The best-fit model, shown with the solid line, has a $\chi^2/\mathrm{dof} = 1.04$. Right: Evolution of effective temperature for SN 2005ay. Blue points are the measured temperatures obtained from an SED fit to the Planck function. The dashed black lines represent the model extrapolation anchored at each blue point, while the red dashed line is the effective model pivoted at the weighted average $T(50)$ value. Red points are the sampled model temperatures at the photometric epochs.

Table 3
Summary of the IIP Parameters and Best-fit EPM Distance and t_0

SN	$v_{\mathrm{phot}}(50)$ (10^3 km s^{-1})	$T(50)$ (10^3 K)	t_0(days)		Distance(d) (Mpc)				Median Distance from NED[a] (Mpc)
							(syst.)		
			Fit	(stat.)	Fit	(stat.)	Total uncorr.	Total corr.	
SN2004gy	4.5 ± 0.2	5.2 ± 0.2	−3.88	1.36	115.78	6.39	12.04	6.06	NA
SN2005ay	3.9 ± 0.1	4.8 ± 0.1	−0.17	0.55	22.33	0.54	3.62	1.14	21.9
SN2006bj	4.4 ± 0.2	8.5 ± 0.3	−0.83	1.27	144.32	9.39	24.07	7.77	NA
SN2006bp	4.3 ± 0.1	4.6 ± 0.2	−0.23	0.66	20.56	0.52	1.76	1.07	17.5
SN2008bj	5.2 ± 0.2	6.2 ± 0.2	3.58	0.77	88.95	3.39	11.62	4.36	NA
SN2008gd	4.9 ± 0.2	6.4 ± 0.3	−3.76	2.58	211.67	21.19	32.17	10.96	NA
SN2008in	2.7 ± 0.1	5.5 ± 0.2	0.34	0.35	16.10	0.21	2.65	0.82	16.6
SN2009dd	3.7 ± 0.1	4.6 ± 0.2	−2.64	0.32	15.36	0.20	0.88	0.81	10.9
PTF10gva	5.2 ± 0.3	6.5 ± 0.2	−1.12	1.33	149.11	7.60	8.62	7.77	NA
SN2013ab	4.2 ± 0.2	4.9 ± 0.2	−1.59	0.44	26.23	0.51	2.96	1.36	23.5
SN2013bu	3.6 ± 0.1	3.7 ± 0.2	1.46	1.05	20.52	1.02	1.54	1.20	14.4(host)
SN2013ej	4.3 ± 0.1	5.5 ± 0.2	−1.18	0.40	9.57	0.17	0.29	0.49	9.5

Notes. The best-fit distances and t_0 values for the 12 SNe IIP with respective statistical uncertainties from the EPM fits are given. Also shown are the total uncorrelated and correlated uncertainties for each of the distance measurements for the SN sample. In the rightmost column, median distances from the NED catalog are also given for those SNe that have distances from redshift-independent measurements. If no SN distance is available, host distances are given for reference whenever available.
[a] Redshift-independent distances from https://ned.ipac.caltech.edu/.

velocity evolution, for events with multiple spectra, the final temperature evolution is derived from the weighted mean $T(50)$ value. The estimated $T(50)$ is then used to anchor the model to desired photometric epochs. The evolving temperatures are sampled from this model at the ROTSE photometric epochs between +7 days and +35 days. The statistical uncertainty for each SN is propagated as an uncorrelated systematic uncertainty from the temperature evolution into the distance error budget. The measured temperatures, the extrapolation models, and the respective final estimates at the ROTSE epochs for SN 2005ay are shown in the right panel of Figure 9. For each SN in the sample, we propagate the extrapolation model uncertainty as a correlated systematic uncertainty from this common temperature evolution model in the final distance error estimates. Table 3 shows the derived +50 day values of the photospheric velocity and the effective temperature for all 12 SNe in our IIP sample.

6. Distance Measurement

We have established the overall methodology and the various inputs that will go into our measurement of SN distance. The photometric measurements and their relationships with the EPM parameters are discussed in Section 4. The best-fit distance for each SN is estimated by χ^2 minimization using Equation (19). We next identify systematic effects that could impact our results and assess their magnitude on the final measurements. As we have modeled both the temperature and the photospheric velocity anchored at the 50 day estimate, in each case, there are two categories of systematic uncertainties that are propagated to the final distance estimation. One is the

uncorrelated systematic uncertainty from the uncertainty on the respective 50 day value, while the other is the correlated systematic uncertainty from the modeling of those parameters at the photometric epochs of each SNe. Both of these uncertainties are propagated to the distance systematic uncertainty. The uncertainties in the galactic extinction (based on Schlafly & Finkbeiner 2011) and the host extinction $E(B-V)$ are also transformed as uncorrelated systematic uncertainty in distance. The additional systematic uncertainty from the K-correction modeling is also propagated from the posterior estimate from the Gaussian Process regression. Finally, we also propagate the uncorrelated systematic uncertainties on the adopted t_0, which are given in Table 1. Better-constrained shock breakout times can significantly reduce the total uncertainty on the distance estimated with the EPM method. The fitted EPM distance and t_0 with the respective uncertainties from the fit are given in Table 3. All epochs including the fitted values of t_0 are relative to the adopted t_0 values in MJD from Table 1. We also note that the uncertainties on t_0 from the fit are consistent with our adopted uncertainties in Table 1.

The systematic uncertainties in distance are also shown in Table 3, where the total uncorrelated systematic uncertainties in distance are calculated from the t_0, $E(B-V)$, z uncertainties and the uncorrelated uncertainties from the velocity and temperature evolution models, all added in quadrature. The total correlated systematic uncertainty includes the contributions from the velocity and temperature evolution models, added in quadrature. Figure 10 shows the best-fit estimated distance measured for each SN in our sample. In each of the SNe shown, the measured data points are given at the ROTSE photometric epochs and the solid lines represent the best-fit solution using Equation (19).

7. Cosmological Analysis

Using the luminosity distances derived above, we employ two methods to extract the Hubble constant (H_0) for the nearby Universe. In one approach, we simulate the impact of peculiar velocities on a sample of 12 galaxies with distances according to the observed distribution and fit for H_0. We also use a Markov Chain Monte Carlo (MCMC) method to obtain a parametric estimation of H_0. In our analysis, we assume no sensitivity of our measurements to other cosmological parameters such as Ω_M and Ω_Λ. In each of these methods, we initially blind the fitted (H_0) parameter by translating with an unknown random additive scalar, then we unblind it at the end to obtain the final estimate.

7.1. Linear Fit of H_0

Peculiar velocities complicate the extraction of H_0 from the sample, and they are substantial relative to recessional velocity for the lower-redshift constituents of this survey. We attempt to mitigate this impact by simulating and fitting galaxies with peculiar velocities at the distances we have calculated. Recessional velocities are simulated according to

$$v = H_0 d, \tag{22}$$

where H_0 is a parameter that can be specified, and we note that this linear relationship holds for the redshift range considered here. We first simulate individual pseudo-experiments populated by SNe distributed according to the distances in Table 3. The recessional velocity for each galaxy in a pseudo-experiment is determined using Equation (22).

Peculiar motion is modeled for each simulated galaxy by adding a random velocity component from a Gaussian distribution centered around 300 km s^{-1}, as is typically quoted in peculiar velocity studies (e.g., Kessler et al. 2009; Davis et al. 2011; Johnson et al. 2014). Each generated peculiar velocity is multiplied by a random value between -1 and 1 to account for the component along the line of sight. Errors in distance for the simulated galaxies are chosen to reflect the data sample uncertainties. Errors in velocity are set to 300 km s^{-1}. We split the analysis using a boundary at $cz_{\rm CMB} = 3000$ km s^{-1}, to distinguish whether the peculiar velocity is large compared to the total velocity. The *local* sample consists of pseudo-experiments that each include seven galaxies with random distances of $5 \leqslant d \leqslant 30$ Mpc. The $H-$flow sample is comprised of pseudo-experiments that each include five galaxies with random distances of $70 \leqslant d \leqslant 260$ Mpc. We then fit Equation (22) to each pseudo-experiment, with H_0 as a free parameter forced to 0 at $z = 0$.

We test this fitting approach for potential bias on the extracted H_0 measurement. We generate 10,000 pseudo-experiments for both samples, repeating this process for input cosmologies of $50 \leqslant H_0 \leqslant 90$ km s^{-1} Mpc^{-1} at 5 km s^{-1} Mpc^{-1} intervals. We calculate the measured value, $H_0^{\rm meas}$, averaged over all pseudo-experiments of each ensemble with the specific input value, $H_0^{\rm true}$. We apply a linear fit to $H_0^{\rm meas}$ versus $H_0^{\rm true}$ and obtain the value of the slope to be 1.0011 ± 0.0007 and that of the intercept to be 0.0651 ± 0.0462, for the *local* sample. The corresponding fit parameters for the $H-$flow sample are 1.0012 ± 0.0007 and 0.0669 ± 0.0451, respectively. These fits yield a slope and offset close to 1.0 and 0.0, respectively, for both the *local* and $H-$flow samples, indicating small but non-negligible bias. Using the fit parameters, we construct calibration vectors with values for each instance of input $H_0^{\rm true}$. The overall $H_0^{\rm meas}$ values for the "*combined*" sample are taken to be the weighted average of the *local* and $H-$flow sample measurements after the respective calibrations. A linear fit of $H_0^{\rm meas}$ versus $H_0^{\rm true}$ for the *combined* sample results in a slope and offset of 0.9999 ± 0.0005 and 0.0005 ± 0.0371, respectively, indicating an adequate mitigation. Differences between $H_0^{\rm meas}$ and $H_0^{\rm true}$ values, ΔH_0, before and after calibration are shown in Figure 11 for a range of tested H_0 values. The small estimated bias for each subsample and the efficacy of the corrections for the combined result are independent of H_0.

We apply the above procedure to the data, using the calibration vectors described above, for the *local* and $H-$flow samples, respectively. We obtain calibrated values of $H_0 = 67.4 \pm 11.8$ (stat) km s^{-1} Mpc^{-1} for the *local* sample and $H_0 = 75.6 \pm 5.1$ (stat) km s^{-1} Mpc^{-1} for the $H-$flow sample. The combined, weighted average yields a final value of $H_0 = 74.3 \pm 4.7$ (stat) km s^{-1} Mpc^{-1}. The Hubble diagram from the fits of *local*, $H-$flow, and the final estimates are shown in the top panel of Figure 12. The blue and magenta dashed lines correspond to the fits to the *local* and $H-$flow samples, and the red line corresponds to the combined weighted estimate. The vertical error bars include the total uncorrelated uncertainty shown from Table 3 added in quadrature with the estimated distance uncertainty from 300 km s^{-1} fixed peculiar velocity, while the horizontal error bars represent that peculiar velocity uncertainty.

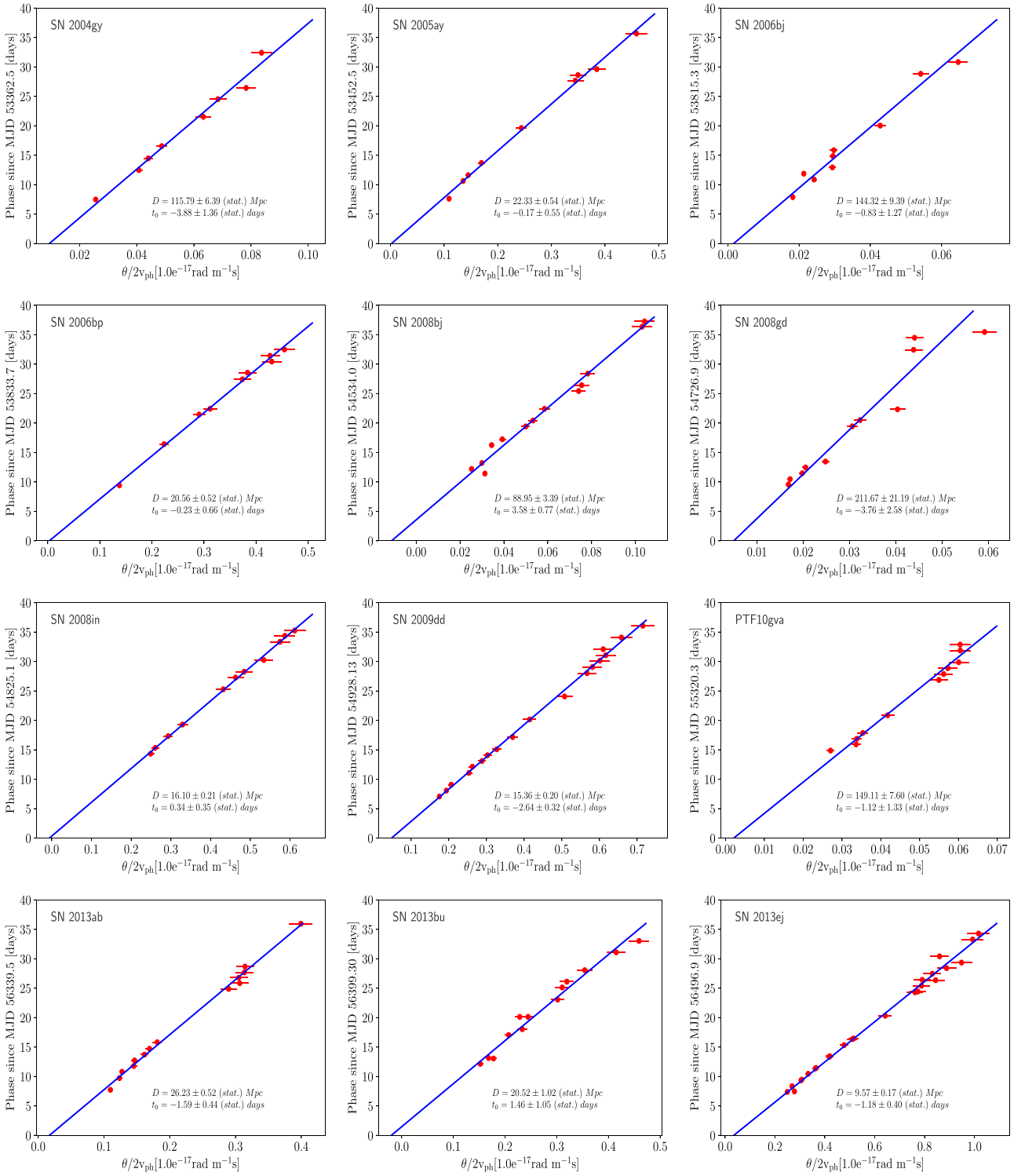

Figure 10. Distance estimates of the 12 ROTSE SNe IIP using the EPM method. In each case, for the SNe shown, the measured data points are given at the ROTSE photometric epochs and the solid lines represent the best-fit solution using Equation (19).

We assess an additional systematic uncertainty due to the correlated impact among the SNe from the velocity and temperature evolution model uncertainties. We add up the correlated errors from Table 3 for all SN distances and refit for H_0. Next, we shift the SN distances lower by subtracting the correlated errors and refit for H_0. The uncertainty on H_0 is calculated from the differences of these fits from the nominal H_0 value. This results in a modeling uncertainty of $^{+4.1}_{-3.7}$ km s^{-1} Mpc^{-1}. A systematic uncertainty due to the assumption of typical peculiar velocity of 300km s^{-1} was assessed by resimulating ensembles with $H_0 = 60$, 70, 80 km s^{-1} Mpc^{-1} for distributions of peculiar velocity centered

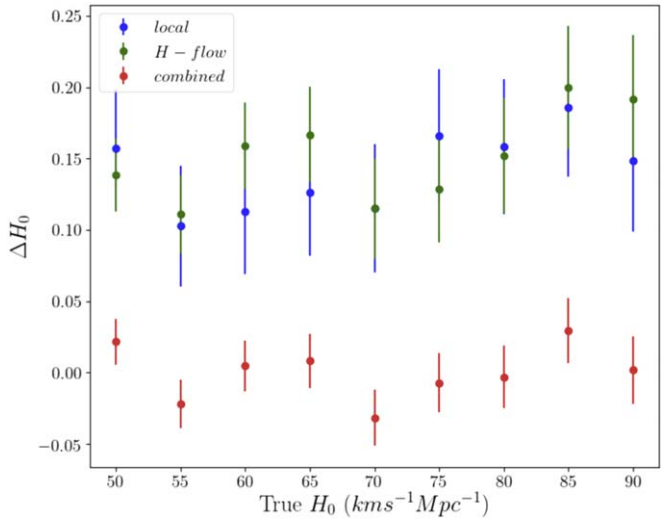

Figure 11. Residuals of average $H_0^{\rm meas}$–$H_0^{\rm true}$, ΔH_0, for the simulated local and $H-$flow samples before calibration, and the *combined* sample after calibration. See text for the slopes and offsets.

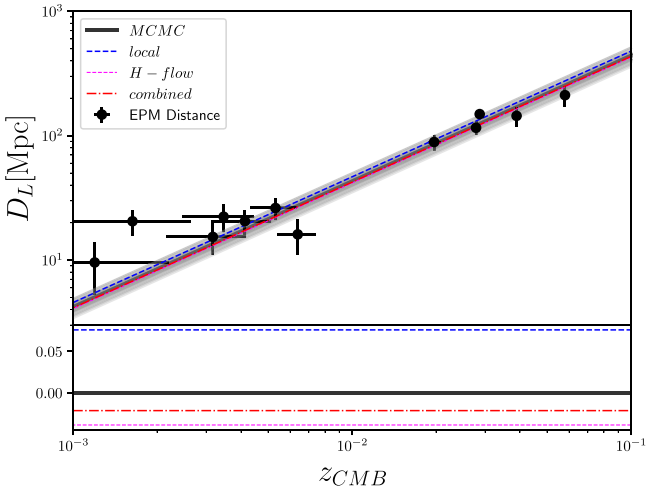

Figure 12. Top: Hubble diagram showing the posterior samples from MCMC in gray. The solid black line is the maximum likelihood estimate from the MCMC method. The black points represent the measured luminosity distances using EPM. The blue and magenta dashed lines correspond to the linear fits to the *local* and $H-$flow samples, and the red curve is the combined weighted estimate from the linear analysis. The horizontal error bars on the data points correspond to the assumed peculiar velocity of 300 km s^{-1}. Bottom: Residuals of the linear fits with respect to the best-fit estimate from the MCMC analysis, shown as differences of log values.

around 230 and 370 km s^{-1} to estimate the lower and upper bounds of potential values of H_0 and peculiar velocity. This yielded an uncertainty of ± 0.3 (sys) km s^{-1} Mpc^{-1}.

7.2. Markov Chain Monte Carlo Sampling

We also perform a parametric estimation of a cosmological model using an MCMC simulation in a Bayesian framework. For the given values of ($z_{\rm CMB}$, Ω_M, Ω_Λ), the luminosity distance (D_L) is given by

$$D_L = \frac{c}{H_0}\int_0^{z_{\rm CMB}} \frac{dx}{\sqrt{\Omega_M(1+x)^3+\Omega_\Lambda}}. \tag{23}$$

We use the publicly available package EMCEE (Foreman-Mackey et al. 2013), where the MCMC is performed to sample the posterior probability distribution obtained from the given likelihood function and the distribution of the priors. We expand the 1D likelihood function discussed previously in D'Andrea et al. (2010), Poznanski et al. (2010), and de Jaeger et al. (2017), in two-dimensional matrix form:

$$\ln\mathcal{L} = -\frac{n}{2}\ln(\det(V)) - \frac{1}{2}\sum_{\rm i=1}^{n}(D_i^{\rm ms} - D_{Li})\,V^{-1}\,(D_i^{\rm ms} - D_{Li}), \tag{24}$$

where the sum is over ($n = 12$) SNe in the sample. Here, $D_i^{\rm ms}$ is the measured distance using EPM, and D_{Li} is the luminosity distance using Equation (23) for the ith SN. The matrix V is given as

$$V = C + \sigma_{\rm int}^2 I, \tag{25}$$

where C is the covariance matrix and $\sigma_{\rm int}$ is the residual intrinsic uncertainty that includes any unaccounted uncertainty in the analysis. The diagonal terms of the covariance matrix C comprise the statistical uncertainties added in quadrature with the total uncorrelated systematic uncertainties from the Table 3, while the off-diagonal terms are computed by multiplying the total correlated systematic errors for respective SNe from Table 3. As in the linear fit analysis, we add in quadrature an uncorrelated uncertainty of 300 km s^{-1} in the diagonal terms to account for the contribution due to peculiar motion.

We consider a flat Universe ($\Omega_M + \Omega_\Lambda = 1; \Omega_M = 0.3$) as our prior. The only free parameters are the Hubble parameter (H_0) and the intrinsic uncertainty $\sigma_{\rm int}$. Now we are not only interested in the best-fit values of these parameters, but also in their full maximum a posteriori probability density distribution. In the Bayesian framework, the joint posterior probability function for these parameters can be written as

$$p(H_0, \sigma_{\rm int}|z_{\rm CMB}, D_L, C, \Omega_M, \Omega_\Lambda) \propto p(H_0, \sigma_{\rm int})p(D_L|z_{\rm CMB}, C, H_0, \sigma_{\rm int}, \Omega_M, \Omega_\Lambda). \tag{26}$$

The function $p(D_L|z_{\rm CMB}, C, H_0, \sigma_{\rm int}, \Omega_M, \Omega_\Lambda)$ is the likelihood function $\mathcal{L}$ given in Equation (24), while for the prior distribution, $p(H_0, \sigma_{\rm int})$, we chose flat priors given by

$$50\ {\rm km\ s^{-1}\,Mpc^{-1}} < H_0 < 150\ {\rm km\ s^{-1}\,Mpc^{-1}} \tag{27}$$

$$0\ {\rm Mpc} < \sigma_{\rm int} < 50\ {\rm Mpc}. \tag{28}$$

We first evaluate the best-fit maximum likelihood estimation (MLE) values of H_0 and $\sigma_{\rm int}$ by minimizing the negative log of the likelihood in Equation (24). Next, we initialize the MCMC chains by picking 500 random initial points as seeds by sampling a small 2D Gaussian ball about the MLE of the parameters H_0 and $\sigma_{\rm int}$. The MCMC is performed using the EMCEE framework for 500 steps for each walker, resulting in a joint posterior probability distribution $p(H_0, \sigma_{\rm int})$. To avoid any systematic sampling bias from the choice of initialization, we discard the first 50 steps of each walker, after which the walkers begin to fully span the full posterior distribution.

The resulting Hubble diagram from the posterior samples is shown in the top panel of Figure 12. The solid black line represents our best-fit model from the MCMC analysis, and the gray lines represent the posterior samples from the MCMC

runs. The black data points are the measured luminosity EPM distances for the SNe IIP sample. The vertical and horizontal error bars are described in Section 7.1. From the final marginalized 1D posterior distributions, the Hubble parameter is estimated to be $72.9^{5.7}_{-4.3}$ km s^{-1} Mpc^{-1} and the intrinsic scatter $\sigma_{\rm int}$ is estimated to be $0.3^{0.42}_{-0.26}$Mpc. The bottom panel of Figure 12 shows the residuals of the obtained fits from the linear analysis in Section 7.1 relative to the best fit from the MCMC analysis shown in the difference of log values.

8. Results and Discussion

Our aim has included development of a methodology for distance measurement of SNe IIP utilizing unfiltered CCD photometry and a minimal number of epochs with color (SED) and spectroscopic data; a method that would enable a sensitive probe of cosmic expansion. We have addressed this previously for SN 2013ej (Dhungana et al. 2016), which was far from the host nucleus and did not require an image-differencing approach. However, analysis of a more representative survey of SNe IIP required a more general approach.

The new image-differencing algorithm, ImageDiff, introduced in this paper was designed to obtain photometric measurements with high efficiency and consistency over a wide range of host environments. It also delivered photon-limited measurements unimpacted by artifacts and their attendant systematic uncertainties. The performance was assessed by injecting PSFs into an image with a full range of SN-nucleus displacements. This showed that we could extract the simulated magnitudes precisely up to a limiting magnitude of ∼18 and across a wide field of view. The performance study showed no significant bias in the photometric residuals, as shown in Figure 2. The new software demonstrated improved photometric detection efficiency up to 20%. By examining SN 2004gk, a typical SN with a distance to the host nucleus of ∼3″, we are able to quantify the improvement over the prior image-differencing code for ROTSE. The scatter in points around the known lightcurve is reduced by approximately three times to roughly 0.1 magnitude (Section 3.1.3) when compared to prior approaches used for the ROTSE SNe data reduction pipeline. The increased performance was particularly observed in the crowded fields and when the SN was closer to the host nucleus. We also note that, for similar image sizes in most cases, the performance across several kernel bases was similar. These results are critical to what follows because the astrophysical and distance measurements produced in this study rely on minimizing photometric uncertainties overall.

In Dhungana et al. (2016), we demonstrated with SN 2013ej the ability to calibrate well the ROTSE unfiltered photometry to a pseudo-bolometric magnitude in order to facilitate the EPM extraction of distance. Such a method requires substantial color photometry spanning from the near-ultraviolet to near-infrared wavelengths at various epochs of the supernova. While that method yielded excellent photometry and an accurate distance measurement, we have attempted a different approach here that relied less on such extensive filtered photometry and spectroscopy by calibrating the ROTSE magnitude to the *V*-band magnitude and using color-based temperature estimates to improve the correction. We also established a *V*-band calibration for the ROTSE unfiltered SNe lightcurves that were consistent with the observed *V*-band SNe lightcurves from the literature. In the end, the correlation with an actual *V*-band mag, at 0.01 magnitudes, is of sufficient precision to obtain accurate distances while keeping the extent of the required broadband photometry and spectroscopy to a minimum.

Utilizing filtered photometry and spectroscopy for several well-measured SNe IIP, we saw that the velocity and temperature evolution exhibited similar behaviors. To quantify this evolution and provide a model from which these properties can be determined at any epoch, we established empirical calibrations for both properties' evolutions using single-epoch photometric and spectroscopic measurements (Section 5). The exponential decay behavior has been empirically observed in the literature of SNe IIP, but its physical origin appears to require further study. Modeling of the photospheric velocity evolution from the spectra indicates that the use of Fe II lines only, such as in Faran et al. (2014), does not accurately describe the early behavior when extrapolated. Using Fe II when observed and He II and H-alpha lines during early times makes the decline in velocity less steep, in agreement with observed SNe (Section 5.2.2). This model also seems to improve the agreement with data sufficiently late in the plateau. Velocities measured for our IIP sample ranged from 2700 km s^{-1} to 5200 km s^{-1} at $t = 50$ d. Remarkably, when normalizing values from other epochs to this value, the behaviors for different events present a very precise exponential fall-off with t, supporting the ability to calibrate the evolution from measurement at a single epoch. Interestingly, the temperature evolution appears to be described well by a similar exponential profile. The temperatures at 50d range widely from 3700 to 8500 K, and yet the evolution lines up well—with the exception of SN 2005cs, which is slightly steeper at early times and flatter than other SNe later. SN 2005cs has been studied very well in the literature, and it appears to be an outlier from the general population, as an underluminous SN. Nevertheless, the four SNe we examined yielded a good fit to Equation (21). While we observed that these models yielded estimates for the velocity and temperature with high precision using very well-sampled SNe, we stress on the importance of a well-constrained t_0 while applying these models, as t_0 is one of the major contributors of the systematic uncertainty.

Use of the EPM technique for distance measurements provided additional constraints on the supernova itself via the fit to t_0. The precision yielded was as small as ±8 hr. The fitted t_0 from the EPM were found to be consistent with our initially adopted values of t_0. We were able to calculate the luminosity distance with limited unfiltered photometry and spectroscopy. Distances ranged from 9.57 ± 0.17(stat.) ± 0.29(uncorr.) $\pm$ 0.49(corr.) to 211.67 $\pm$ 21.19(stat.) $\pm$ 32.17(uncorr.) $\pm$ 10.96(corr.)Mpc. As shown in Table 3, these distance measurements agree with those in the literature from the host galaxies.

The precise calibration of astrophysical properties using a single measurement epoch, as in several of these SNe, can be a powerful advantage of the EPM over other techniques, where the observations need not only to be densely sampled but also require concurrent multi-band photometry. Given the potential challenges of observing with large-pitch, unfiltered CCDs, the measurements in Figure 10 are remarkably linear through the entire range of epochs chosen for all of the SNe in this sample. Dense sampling during the plateau phase increases statistics and could reduce the EPM uncertainties. However, the low scatter of points around these slopes, which arises in part from the low scatter of points around the physical

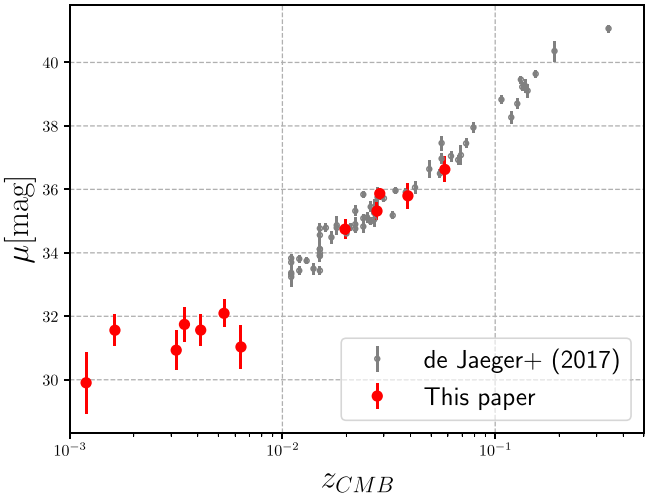

Figure 13. Distance moduli for the 12 SNe in our sample using the EPM method are overlaid on top of the SCM measurements from de Jaeger et al. (2017). The distance uncertainties for our sample include the contribution from flat peculiar velocity of 300 km s^{-1} along with the statistical and total uncorrelated uncertainties from Table 3, added in quadrature.

parameter evolution models, suggests observables have strong correlations and numerous concurrent observations are not absolutely necessary for the EPM measurements.

These results strongly suggest a robustness of the method to the choice of plateau span utilized. In particular, stripped core supernovae of types Ib and Ic that lack extensive plateaus might be viable in this method using a shorter time duration. Such a possibility was already explored in Vinkó et al. (2004) with SN 2002ap. We have also obtained a preliminary result for 2007gr in Staten (2020). Both yielded distances to their hosts in agreement with the literature.

Our analysis shows an inherent promise of the EPM method, whose very general physical assumptions have allowed us to leverage unfiltered photometry with minimal spectroscopy and color information. In fact, the results indicate that SNe with only one epoch of either performed similarly to those with three or more epochs when using the normalized, exponential time-evolution models described in Section 5. Our results can also be obtained by using *V*-band photometry in place of the unfiltered photometry. We note that, while the accurate systematics from the dilution parameter may affect the distance results, some limitation in their magnitude can be inferred from the linearity of the EPM plots over the whole plateau, as well as from the validity of the SNe IIP distances compared to those of their hosts. Further work, where the uncertainties will be reduced overall, will necessitate more careful handling of this issue. Figure 13 shows the EPM distance modulus derived for our SN sample overlaid on top of those measured from the SCM technique by de Jaeger et al. (2017) (see Figure 5 in their paper). On the overlapping redshift range, the distances measured from independent methods and samples are statistically consistent.

A driving motivation in the current study was to test cosmic expansion in the local Universe. The linear method we used has the advantage that it makes no cosmological assumption and allowed us to estimate and mitigate the effects from peculiar motion via a simple simulation. As such, it yielded consistent values of $H_0 = 67.4 \pm 11.8$(stat.)km s^{-1} Mpc^{-1} and $H_0 = 75.6 \pm 5.1$(stat.) $\pm$ 0.3 (syst.) km s^{-1} Mpc^{-1} in the *local* and $H-$flow regimes, respectively, with very different relative sizes of peculiar velocities to cosmic recession. The combined measurement yields $H_0 = 74.3^{+4.7}_{-4.7}$ (stat.)$^{+4.1}_{-3.7}$ (syst.) $\pm$ 0.3 (Pec. Vel.) km s^{-1} Mpc^{-1}. The impact of peculiar velocities is minimal. We can also see that, with only 12 SNe, our results are already almost dominated by systematics. Future work will require more effort to reduce systematic effects.

The MCMC method we employed presented different advantages for this analysis. The technique jointly estimates the posterior distribution for H_0 and a measure of intrinsic residual systematic uncertainty $\sigma_{\rm int}$ for the analysis. We utilize the full information in the covariance matrix, and the approach provides a test of unknown contributions to the scatter of points. The value returned, corresponding to $0.3^{+0.42}_{-0.26} Mpc$, is consistent with zero. We obtain a measurement for the full sample of 12 SNe of $H_0 = 72.9^{+5.7}_{-4.3}$ km s^{-1} Mpc^{-1}, which is in excellent agreement with the result from the linear method. Even though we have fixed other cosmological parameters, it is interesting to note that the residual intrinsic dispersion we find from the analysis of our SNe IIP sample is not statistically significant.

For a quick test, we repeated the MCMC analysis using the five events from the $z > 0.01$ sample but dropping the peculiar velocity from the uncorrelated diagonal error term. This choice of cutoff is ubiquitous in the literature, including the SNe Ia studies. The contribution from the galactic peculiar motion at such redshift is expected to be $\sim$10% or less (e.g., Kessler et al. 2009). In such a limited sample, we observe no statistically significant shift in either H_0 or $\sigma_{\rm int}$. Because we incorporated the correlated systematic uncertainties within the covariance matrix of the distances in the MCMC analysis, we take this estimate as our final estimation for H_0.

When comparing to the other probes such as SNe Ia measurements from recent DES results (Abbott et al. 2019), we see that our results are in good agreement. We also find our estimated H_0 value to be consistent with that obtained from the CMB measurements (Planck Collaboration et al. 2016) at the 1σ level. In the future, our measurement could be substantially improved by a larger sample, as well as by more careful consideration of the underlying time-evolution modeling and correlations among SNe we have utilized.

9. Conclusion

We performed an end-to-end analysis of the time evolution of SNe IIP properties and of the measurement of cosmological properties in the EPM framework using photometric and spectroscopic observations of a sample of 12 SNe IIP. We significantly improved the ROTSE SNe photometry sampling and precision with new image differencing for ROTSE SNe images using a kernel convolution technique.

In our analysis of SNe IIP, we have established excellent performance of unfiltered CCD photometry, including in areas crowded by host nuclei, to yield valuable measurements of supernova properties and to measure cosmic expansion in the nearby Universe. We demonstrated a broad consistency between SNe IIP of the time evolution of event ejecta velocities and photospheric temperatures from the times of peak luminosity throughout most of the plateau among these diverse SNe. From well-sampled SNe photometry with precise estimation of explosion epoch, we empirically established time-evolution models to extrapolate the photospheric velocity and temperature from as few as a single photometric and

spectroscopic measurement. Using the EPM technique, we obtained the luminosity distances for each SN. These distance measurements are in good agreement with host distances in the literature, and the linearity of the EPM diagrams suggests the viability of further generalization of this approach. Overall, the EPM technique looks promising to pursue cosmological studies for larger data sets, potentially to even higher redshifts.

Utilizing two approaches to fitting for H_0, we have obtained a measurement of $H_0 = 72.9^{+5.7}_{-4.3}$ km s^{-1} Mpc^{-1}. We further established that unknown peculiar velocities do not significantly impact this measurement. Results from an MCMC approach also indicate that we have accounted for all appreciable contributors (and their uncertainties) to the scatter of points.

Acknowledgments

R.K. wishes to thank NASA for grant NNX10A196H (P.I. Kehoe), and the Dean's Research Council of SMU for supporting the initial work for this paper. J.C.W. and J.V. are supported in part by NSF AST-1813825. J.V. and his group at Konkoly Observatory are supported by the project "Transient Astrophysical Objects" GINOP 2.3.2-15-2016-00033 of the National Research, Development and Innovation Office (NKFIH), Hungary, funded by the European Union. We would like to acknowledge the McDonald Observatory technical and observation support crew for tremendous help during the ROTSE and HET observations over the years. We would also like to thank Jeffrey Silverman for useful discussions on the data processing and analysis.

ORCID iDs

G. Dhungana https://orcid.org/0000-0002-5402-1216
R. Kehoe https://orcid.org/0000-0002-7101-697X
J. Vinko https://orcid.org/0000-0001-8764-7832
J. C. Wheeler https://orcid.org/0000-0003-1349-6538
R. M. Quimby https://orcid.org/0000-0001-9171-5236
W. Zheng https://orcid.org/0000-0002-2636-6508

References

Abbott, T. M. C., Allam, S., Andersen, P., et al. 2019, ApJL, 872, L30
Akerlof, C. W., Kehoe, R. L., McKay, T. A., et al. 2003, PASP, 115, 132
Alard, C., & Lupton, R. H. 1998, ApJ, 503, 325
Bailey, S. 2012, PASP, 124, 1015
Becker, A. C., Homrighausen, D., Connolly, A. J., et al. 2012, MNRAS, 425, 1341
Benetti, S., Cappellaro, E., Mazzali, P. A., et al. 2005, ApJ, 623, 1011
Bertin, E., & Arnouts, S. 1996, A&AS, 117, 393
Blondin, S., Dessart, L., Hillier, D. J., et al. 2017, MNRAS, 470, 157
Bolton, A. S., & Schlegel, D. J. 2010, PASP, 122, 248
Bose, S., & Kumar, B. 2014, ApJ, 782, 98
Bose, S., Valenti, S., Misra, K., et al. 2015, MNRAS, 450, 2373
Bramich, D. M. 2008, MNRAS, 386, L77
Branch, D., & Wheeler, J. C. 2017, Supernova Explosions (Berlin: Springer)
Brout, D., Scolnic, D., Popovic, B., et al. 2022, ApJ, 938, 110
Cardelli, J. A., Clayton, G. C., & Mathis, J. S. 1989, ApJ, 345, 245
D'Andrea, C. B., Sako, M., Dilday, B., et al. 2010, ApJ, 708, 661
Davis, T. M., Hui, L., Frieman, J. A., et al. 2011, ApJ, 741, 67
de Jaeger, T., Galbany, L., Filippenko, A. V., et al. 2017, MNRAS, 472, 4233
de Jaeger, T., González-Gaitán, S., Anderson, J. P., et al. 2015, ApJ, 815, 121
DES Collaboration, et al. 2018, PhRvL, 122, 171301
Dessart, L., & Hillier, D. J. 2005, A&A, 439, 671
Dhungana, G. 2018, PhD thesis, Southern Methodist Univ. Dallas, TX
Dhungana, G., & Kehoe, R. 2023, ImageDiff, v1, Zenodo, doi:10.5281/zenodo.10158227
Dhungana, G., Kehoe, R., Vinko, J., et al. 2016, ApJ, 822, 6
Dong, Y., Valenti, S., Bostroem, K. A., et al. 2021, ApJ, 906, 56
Eastman, R. G., Schmidt, B. P., & Kirshner, R. 1996, ApJ, 466, 911
Elmhamdi, A., Tsvetkov, D., Danziger, I. J., & Kordi, A. 2011, ApJ, 731, 129
Faran, T., Poznanski, D., Filippenko, A. V., et al. 2014, MNRAS, 442, 844
Filippenko, A. V. 1997, ARA&A, 35, 309
Fitzpatrick, E. L. 1999, PASP, 111, 63
Foreman-Mackey, D., Hogg, D. W., Lang, D., & Goodman, J. 2013, PASP, 125, 306
Gall, E. E. E., Kotak, R., Leibundgut, B., et al. 2016, A&A, 592, A129
Gall, E. E. E., Kotak, R., Leibundgut, B., et al. 2018, A&A, 611, A25
Gal-Yam, A., Bufano, F., Barlow, T. A., et al. 2008, ApJL, 685, L117
Graur, O., Bianco, F. B., & Modjaz, M. 2015, MNRAS, 450, 905
Guillochon, J., Parrent, J., Kelley, L. Z., & Margutti, R. 2017, ApJ, 835, 64
Hamuy, M., & Pinto, P. A. 2002, ApJ, 566, 63
Hamuy, M., Pinto, P. A., Maza, J., et al. 2001, ApJ, 558, 615
Hatano, K., Branch, D., Fisher, A., et al. 1999, ApJS, 121, 233
Hill, G. J., Nicklas, H. E., MacQueen, P. J., et al. 1998, Proc. SPIE, 3355, 375
Howell, D. A. 2011, NatCo, 2, 350
Inserra, C., Pastorello, A., Turatto, M., et al. 2013, A&A, 555, A142
Johnson, A., Blake, C., Koda, J., et al. 2014, MNRAS, 444, 3926
Jones, M. I., Hamuy, M., Lira, P., et al. 2009, ApJ, 696, 1176
Kasen, D., & Woosley, S. E. 2009, ApJ, 703, 2205
Kelly, P. L., & Kirshner, R. P. 2012, ApJ, 759, 107
Kessler, R., Becker, A. C., Cinabro, D., et al. 2009, ApJS, 185, 32
Kessler, R., Marriner, J., Childress, M., et al. 2015, AJ, 150, 172
Khazov, D., Yaron, O., Gal-Yam, A., et al. 2016, ApJ, 818, 3
Kirshner, R. P., & Kwan, J. 1974, ApJ, 193, 27
Leonard, D. C., Filippenko, A. V., Gates, E. L., et al. 2002, PASP, 114, 35
Marion, G. H., Brown, P. J., Vinkó, J., et al. 2016, ApJ, 820, 92
Nicola, A., Refregier, A., & Amara, A. 2017, PhRvD, 95, 083523
Nugent, P. E., Sullivan, M., Ellis, R., et al. 2006, ApJ, 645, 841
Pedregosa, F., Varoquaux, G., Gramfort, A., et al. 2011, JMLR, 12, 2825
Pejcha, O., & Prieto, J. L. 2015, ApJ, 799, 215
Perlmutter, S., Aldering, G., Goldhaber, G., et al. 1999, ApJ, 517, 565
Phillips, M. M. 1993, ApJL, 413, L105
Rodríguez, Ó., Clocchiatti, A., & Hamuy, M. 2014, AJ, 148, 107
Rodríguez, Ó., Pignata, G., Hamuy, M., et al. 2019, MNRAS, 483, 5459
Planck Collaboration, Ade, P. A. R., Aghanim, N., et al. 2016, A&A, 594, A13
Poznanski, D., Nugent, P. E., & Filippenko, A. V. 2010, ApJ, 721, 956
Quimby, R. M. 2006, PhD thesis, Univ. Texas, Austin, TX
Quimby, R. M., Wheeler, J. C., Höflich, P., et al. 2007, ApJ, 666, 1093
Riess, A. G., Filippenko, A. V., Challis, P., et al. 1998, AJ, 116, 1009
Roy, R., Kumar, B., Benetti, S., et al. 2011, ApJ, 736, 76
Schlafly, E. F., & Finkbeiner, D. P. 2011, ApJ, 737, 103
Schmidt, B. P., Kirshner, R. P., Eastman, R. G., et al. 1994, ApJ, 432, 42
Silverman, J. M., Foley, R. J., Filippenko, A. V., et al. 2012, MNRAS, 425, 1789S
Staten, R. 2020, PhD thesis, Southern Methodist Univ., Dallas, TX
Szalai, T., Vinkó, J., Könyves-Tóth, R., et al. 2019, ApJ, 876, 19
Tripp, R. 1998, A&A, 331, 815
Valenti, S., Howell, D. A., Stritzinger, M. D., et al. 2016, MNRAS, 459, 3939
Van Dyk, S. D., Zheng, W., Maund, J. R., et al. 2019, ApJ, 875, 136
Vinkó, J., Blake, R. M., Sárneczky, K., et al. 2004, A&A, 427, 453
Vinkó, J., Takáts, K., Szalai, T., et al. 2012, A&A, 540, A93
Vogl, C., Sim, S. A., Noebauer, U. M., et al. 2019, A&A, 621, A29
Weinberg, D. H., Mortonson, M. J., Eisenstein, D. J., et al. 2013, PhR, 530, 87W
Yaron, O., & Gal-Yam, A. 2012, PASP, 124, 668
Yuan, F. 2010, PhD thesis, Univ. Michigan, Ann Arbor, MI
Yuan, F., & Akerlof, C. 2008, ApJ, 677, 808